nature communications

Article

https://doi.org/10.1038/s41467-026-68466-5

Leveraging glucan-induced trained immunity for the epigenetic and metabolic rewiring of macrophages to enhance colorectal cancer vaccine response

Received: 16 April 2025

Accepted: 8 January 2026

Published online: 28 January 2026

Check for updates

Firas Hamdan[1,2,3,4], Sara Gandolfi[4,5,6,16], Federica D'Alessio[1,2,3,4,16], Yvonne Giannoula[1,2,3,4], Julia Kolikova[4,7], Manlio Fusciello[1,2,3,4], Elisa Zaghen[1], Alessandra Napolano[8,9], Salvatore Russo[1,2,3,4], Ozan Izci[1], Paolo Bottega[1,2,3,4], Jacopo Chiaro[1,2,3,4], Kirsi-Marja Alanen[10], Gabriella Antignani[1,2,3,4], Michaela Feodoroff[1,2,3,4,11], Virpi Stigzelius[1,2,3,12], Milda Sakalauskaite[1,2,3,4], Janita Sandberg[1,2,3,4], Anni I. Nieminen[13], Nicola Zambrano[8,9], Ove Eriksson[10], Satu Mustjoki[4,5,6], Toni T. Seppälä[4,7,14,15], Mikaela Grönholm[1,2,3,4] & Vincenzo Cerullo[1,2,3,4,9]

Colorectal cancer (CRC) remains refractory to most immunotherapies, with cancer vaccines failing due to an immunosuppressive tumor microenvironment. Here, we show that β-glucan–induced trained immunity overcomes these barriers by reprogramming macrophages through H3K4me3-dependent epigenetic modifications and metabolic rewiring. In female mice vaccinated with peptide-coated adenovirus-based vaccine PeptiCrad, training enhances glycolysis with creatine metabolism sustaining CXCL9/10 production, enabling macrophages to recruit NK cells via CXCR3. In turn, NK cells produce CCL5, driving cDC1 infiltration and antigen presentation, which together amplify effector memory $CD8^+$ T cell responses. Moreover, with human peripheral blood mononuclear cells and CRC patient-derived organoids, trained macrophages boost NK migration, antigen-specific T cell activation, and tumor killing. These findings highlight trained immunity as a powerful adjuvant to reinvigorate colorectal cancer vaccination.

Colorectal cancer (CRC) has attained significant negative attention due to it being the second-leading cause of cancer-related deaths[1]. Moreover, colorectal cancer is the third most common cancer and the second leading cause of cancer-related deaths worldwide, with an estimated 1.9 million new cases and almost 1 million deaths in 2020[2]. Despite its incidence plateauing or decreasing among older adults due to the widespread use of screening, several studies reported a rise in CRC diagnoses among younger adults globally (under 50 years)[3]. Compared to late onset CRC, younger patients have a higher proportion of advanced stage and, despite significantly better survival rates, the overall survival (OS) in metastatic early onset CRC is 18 months, highlighting the urgent need for improved screening strategies and novel therapeutic approaches[4].

Traditional treatment approaches rely on chemotherapy, radiation and radical surgical resection, which, although effective in a subset of patients, are burdened by various side effects and a high relapse rate of around 70-75%, especially in more advanced CRC cases[4]. A shift in the treatment paradigm occurred when cancer immunotherapies were introduced in the clinic. Significant advances with immune checkpoint inhibitors (ICI) were observed in the treatment of

A full list of affiliations appears at the end of the paper. e-mail: vincenzo.cerullo@helsinki.fi

CRC, especially with mismatch repair deficient CRC or high microsatellite instability owing to higher mutational burden[5–8]. Nevertheless, ICI proved largely ineffective in mismatch repair proficient or microsatellite instability low CRC with, accounting for 85% of all cases[9,10]. To overcome this unmet medical need, various cancer vaccines have been designed to enhance an active anti-tumor T cell response, and several clinical trials have been conducted showing increased overall responses[11–14]. Nevertheless, the tumor microenvironment (TME) was seen as a common factor limiting tumor eradication. Despite the formation of an adequate CD8 + T cell response/infiltration and IFN-γ response, the tumor-killing efficacy has been damped by the presence of T-regs[15–17], myeloid-derived suppressor cells (MDSCs)[18–20], tumor-associated macrophages (TAMs)[21–24] and immunosuppressive cytokines[25–27]. Hence, modulation of the TME could be an effective strategy to enhance cancer vaccines in CRC.

Trained immunity was described by Netea and colleagues as an aspecific memory response of the innate immune system[28]. It involves an epigenetic and metabolomic reprogramming of innate immune cells, when exposed to specific stimuli, resulting in an enhanced response when re-exposed to a heterologous stimulus. Many studies have shown a protection against a heterologous challenge of pathogens including bacteria[29–31], viruses[32–36] or fungi. With respect to cancer, only recently has there been studies implicating tumor cells as stimuli for trained immunity. These effects have been seen in breast[37,38], pancreatic[39,40] and lung cancer where an overall anti-tumor inflammation was noticed in all studies. Specifically, a reduction of MDSC and reprogramming of TAM and monocytes towards anti-tumor have been observed leading to an increase in ICI therapy response[39,40]. Therefore, it is believed that trained immunity could enhance cancer vaccination by modulating the TME, specifically the innate immune populations. Moreover, it also believed that trained immunity could further boost the strength of elicited adaptive immune responses by strengthening the innate immune response. This is a concept that has been hypothesized but never studied.

In this work, we utilize beta-glucan as an inducer of trained immunity and test whether it could enhance the effect of PeptiCrad (PC)[41,42], a cancer vaccine platform in which tumor-specific peptides are electrostatically coated onto the surface of adenoviruses, thereby combining efficient viral delivery with antigen-specific T cell priming. PC is currently under clinical evaluation (NCT05492682). When trained immunity is induced in CRC-bearing mice, vaccination is shown to be enhanced. Metabolomic studies reveal a rewiring of TAMs causing an increase in the Warburg effect and epigenetic changes. Single-cell RNA sequencing reveals that such TAMs upregulate CXCL9 and CXCL10 leading to an increase in NK cell infiltration. This increase of NK cells results in the excretion of CCL5 inducing conventional dendritic cells 1 (cDC1) populations further enhancing T-cell responses. In human studies, we also show that PBMCs induced by trained immunity have higher CD8 + T cells responses when treated with a cancer vaccine leading to an enhanced tumor killing in CRC-patient derived organoids.

Results

Glucan-induced trained immunity enhances vaccine response

To explore the immunological effects of glucan-induced trained immunity, we re-analysed single-cell RNA sequencing data from a previously published study[40]. In that study C57BL/6 mice were treated with either PBS or whole glucan particles derived from cell walls of yeast (WPG), and pancreas tissue was collected at days 3 and 7 post-treatment. Distinct shifts in immune cell populations were observed between PBS- and WPG-treated mice (Fig. 1A, Supplementary Fig. 1A). Notably, clusters 7, 11, and 12 increased progressively in WPG-treated mice (Fig. 1B) and were identified as Chil3 + Ly6C macrophages and monocytes, suggesting their involvement in trained immunity.

Average gene expression revealed increased antigen processing and presentation genes in WPG mice at both time points (Supplementary Fig. 1B–C). *Hif1α*, a hallmark of trained immunity, was also upregulated (Supplementary Fig. 1D). DEG analysis of clusters 7, 11, and 12 confirmed upregulation of antigen presentation genes (Fig. 1C). In cluster 11, *b2m*, *h2-k1*, *ctss*, and h*2-q7* were elevated at day 7 (Fig. 1D–E), while cluster 7 showed increased *ctsc*, h*2-dma*, *h2-ab1*, and *h2-aa*, and cluster 12 upregulated *b2m*. These changes align with enhanced MHC-I and MHC-II pathways, supporting adaptive immune priming. Furthermore, *cxcl9* and *cxcl10* were upregulated (Supplementary Fig. 1E), suggesting increased NK and T cell recruitment. Importantly, this focused analysis of clusters 7, 11, and 12—emphasizing antigen presentation and NK/T cell attraction—was not explored in the original Geller dataset.

Since this analysis was restricted to the pancreas and immune cell populations may differ, we further investigated whether WPG-induced trained immunity could enhance a vaccine response systemically. C57BL/6 mice were pre-treated with PBS or WPG and vaccinated with adenovirus-based PC carrying SIINFEKL (Fig. 1F) as a proof of concept. Flow cytometry revealed that SIINFEKL stimulation induced significant shifts in T cell memory subsets (Supplementary Fig. 2A, and Supplementary Fig. 3A). Trained mice showed reduced central memory (CM) (CD44 + CD62L +) and increased effector memory (EM) (CD44 + CD62L−) CD8 + T cells (Fig. 1G), a phenotype linked to robust responses. Moreover, CD8 + T cells from trained mice expressed higher IFN-γ and TNF-α (Fig. 1H–I), with increased cytokine production per cell (Supplementary Fig. 3B). IL-2 was not elevated (Supplementary Fig. 3C). Additionally, SIINFEKL stimulation induced IL-2, TNF-α, and IFN-γ in CD4 + T cells (Supplementary Fig. 3D), likely reflecting indirect CD8 + T cell effects[43,44]. Together, these results demonstrate that WPG-induced trained immunity enhances antigen presentation in myeloid cells and promotes effector memory CD8 + T cell responses, strengthening vaccine-induced immunity.

Immunity enhances vaccine response in both a prophylactic and therapy settings in CT26 bearing mice

After observing the effects of our initial in vivo vaccine model, we proceeded to test our approach in a colon cancer setting using the CT26 model. To mimic a prophylactic setting, Balb/c mice were first treated with either PBS or WPG (Fig. 2A) before tumor implantation. Following this, we utilized the same adenovirus-based vaccine (PC), this time coated with a validated immunogenic CT26-derived/specific peptide (Syl peptide)[44]. As shown, mice treated with the combination of WPG and PeptiCRAd (Trained+PC) exhibited the strongest tumor control, PC alone showed moderate suppression, and WPG alone had no effect compared to mock (Fig. 2B, Supplementary Fig. 4A). Thus, trained immunity alone was insufficient, but it primed the immune system to enhance vaccine efficacy.

After sacrificing the mice, we analyzed dendritic cell subsets in draining lymph nodes (Fig. 2C, Supplementary Fig. 5A). While cDC2 (CD103- MHCII+ CD11c +) cells dominated across groups, WPG and Trained+PC treatment increased cDC1(CD103 + MHCII+ CD11c +) frequency, with Trained+PC showing the strongest effect.

Next, we next assessed the systemic immune response by isolating splenocytes from treated mice and stimulating them ex vivo with either PBS, adenovirus, or the Syl peptide. With PBS stimulation, Trained+PC mice showed elevated EM T cells in both CD8+ (CD44 + CD62L-) (Fig. 2D) and CD4+ (Fig. 2E) compartments, indicating systemic priming. Upon Syl peptide restimulation, Trained+PC splenocytes again exhibited more EM T cells and fewer CM T cells (CD44-CD62L-) in CD8+ (Fig. 2F) and CD4+ (Fig. 2G) compartments, confirming peptide-specific memory. In contrast, WPG alone failed to induce Syl-specific responses, though splenocytes responded robustly to adenovirus, consistent with trained immunity boosting antiviral pathways.

https://doi.org/10.1038/s41467-026-68466-5

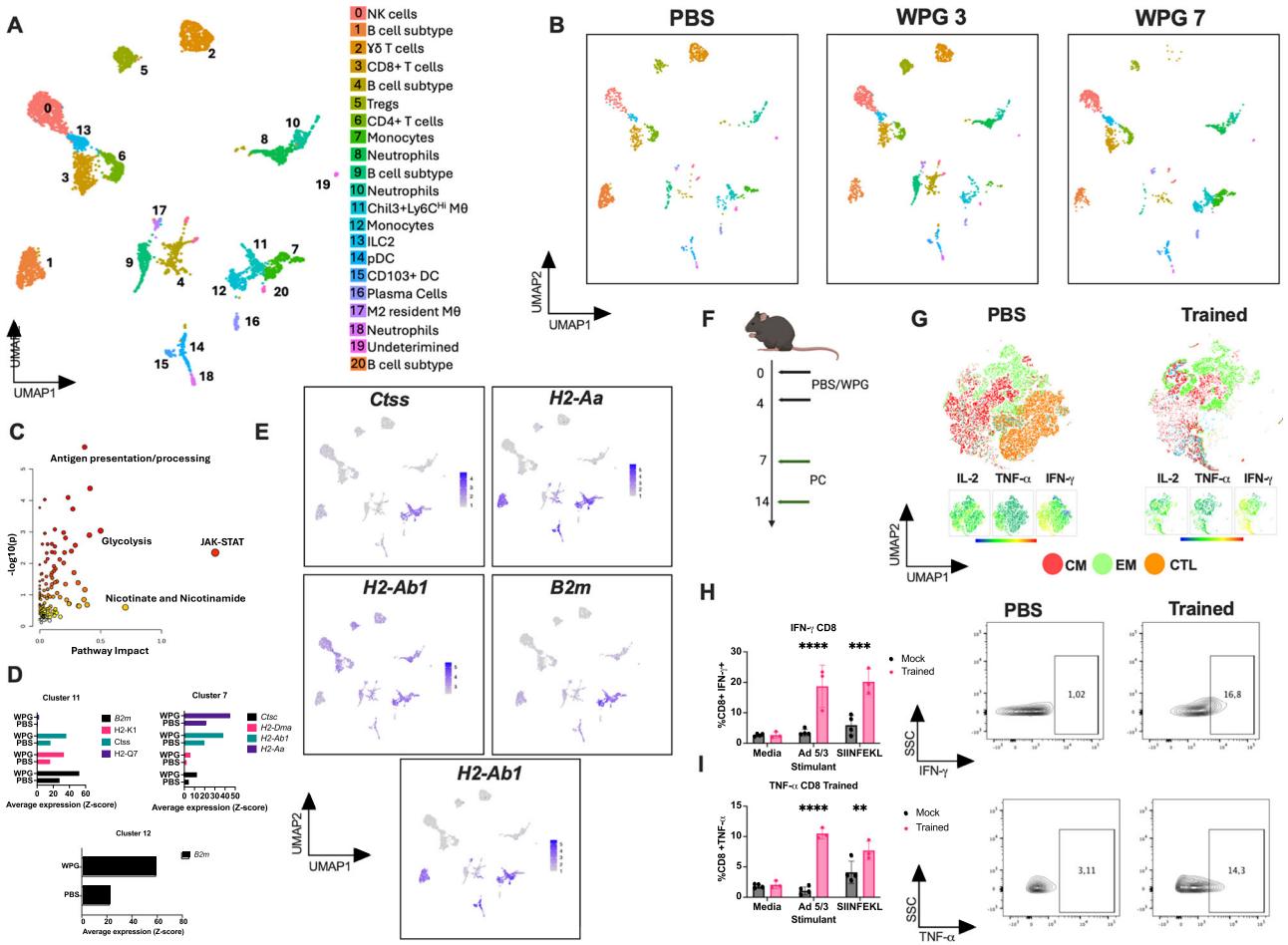

Fig. 1 | WPG stimulates the myeloid compartment to enhanced vaccine responses. Single-cell RNA sequencing data, previously published[40], were re-analysed from mice given PBS ($n = 3$) or WPG ($n = 3$) (sacrificed at day 3 and day 7 post WPG treatment). **A** Two-dimensional UMAP representation of 4803 cells from the three treatment groups aggregated together. **B** UMAP dimension reduced of PBS (1251 cells), WPG 3(2161) and WPG7 (1385). **C** Pathway impact analysis on DEG of clusters 7, 11 and 12. Pathway significance was assessed using a two-sided hypergeometric test with FDR correction **D** Comparison between WPG and PBS in the average expression of antigen presentation genes from clusters 11, 7 and 12. Significance was assessed using a two-sided hypergeometric test; topology based on degree centrality **E** Single cell RNA sequencing data showing a UMAP of expression of *Ctss*, *H2-Aa*, *H2-Ab1* and *B2m* in all clusters in WPG. **F** Schematic of treatment dosage of mice vaccinated with PC (against SIINFEKL) (Created in BioRender. Hamdan, F. (https://BioRender.com/otyn63b). **G** Flow-cytometry data showing a UMAP dimension of different CD8+ memory cells from splenocytes of PBS and WPG treated mice after stimulating with SIINFEKL peptide at day 15. Expression of IL-2, TNF-α and IFN-γ were also mapped in the UMAP obtained from $n = 3$ mice from each treatment group. **H** IFN-γ levels of splenocytes of PBS and WPG treated mice after stimulation with media, Ad5/3 and SIINFEKL peptide obtained from $n = 3$ mice from each treatment group (‘****’ $p < 0.0001$; ‘***’ $p = 0.0023$). Data are the means ± SD. Contour plots are representative images of splenocytes stimulated with SIINFEKL peptide. **I** TNF-α levels of splenocytes of PBS and WPG treated mice after stimulation with PBS, Ad5/3 and SIINFEKL peptide obtained from $n = 3$ mice from each treatment group (‘****’ $p < 0.0001$; ‘***’ $p = 0.0002$). Data are the means ± SD. Contour plots are representative images of splenocytes stimulated with SIINFEKL peptide. Statistical significance was assessed with one-way ANOVA for the flow cytometry analysis along with a Tukey’s multiple comparisons test. Source data are provided as a Source Data file.

To assess therapeutic potential, we tested established CT26 tumors. WPG was administered post-implantation, followed by vaccination (Fig. 2K). Again, Trained+PC mice exhibited the lowest tumor burden (Fig. 2L–M), whereas Mock, PC, or WPG alone had little effect. TME analysis showed increased monocyte (Fig. 2N) and TAM infiltration (Fig. 2O) in Trained and Trained+PC groups, while neutrophils remained unchanged (Supplementary Fig. 6A). TAMs expressed higher CD80 (Supplementary Fig. 6B) and monocytes higher CD86 (Supplementary Fig. 6C), indicating activation.

Together, these results demonstrate that WPG-induced trained immunity enhances CRC vaccination in both prophylactic and therapeutic contexts. This synergy involves expansion of cDC1, systemic effector memory T cell priming, increased cytokine production, and remodeling of the TME to favor monocyte/TAM activation.

Metabolomic profiling of CD11b+ cells reveals metabolic reprogramming

Trained immunity has been previously shown to alter the metabolic function of myeloid cells. To further investigate the metabolic state of tumor-infiltrating CD11b$^+$ cells, we performed a comprehensive metabolomic analysis following treatment. Given that CD11b$^+$ cells are the primary immune population affected by our strategy, we sought to determine how their metabolic landscape changes upon exposure to PC versus WPG combined with PC (Trained+PC). Tumors were harvested, CD11b$^+$ cells were FACS-sorted, and subjected to metabolomic profiling (Fig. 3A, Supplementary Fig. 7A).

Principal component analysis (PCA) revealed distinct clustering between the two groups, with PC1 and PC2 accounting for 62.2% and 24.5% of the variance, respectively (Fig. 3B), highlighting a clear divergence in metabolite composition after Trained+PC. Comparative

https://doi.org/10.1038/s41467-026-68466-5

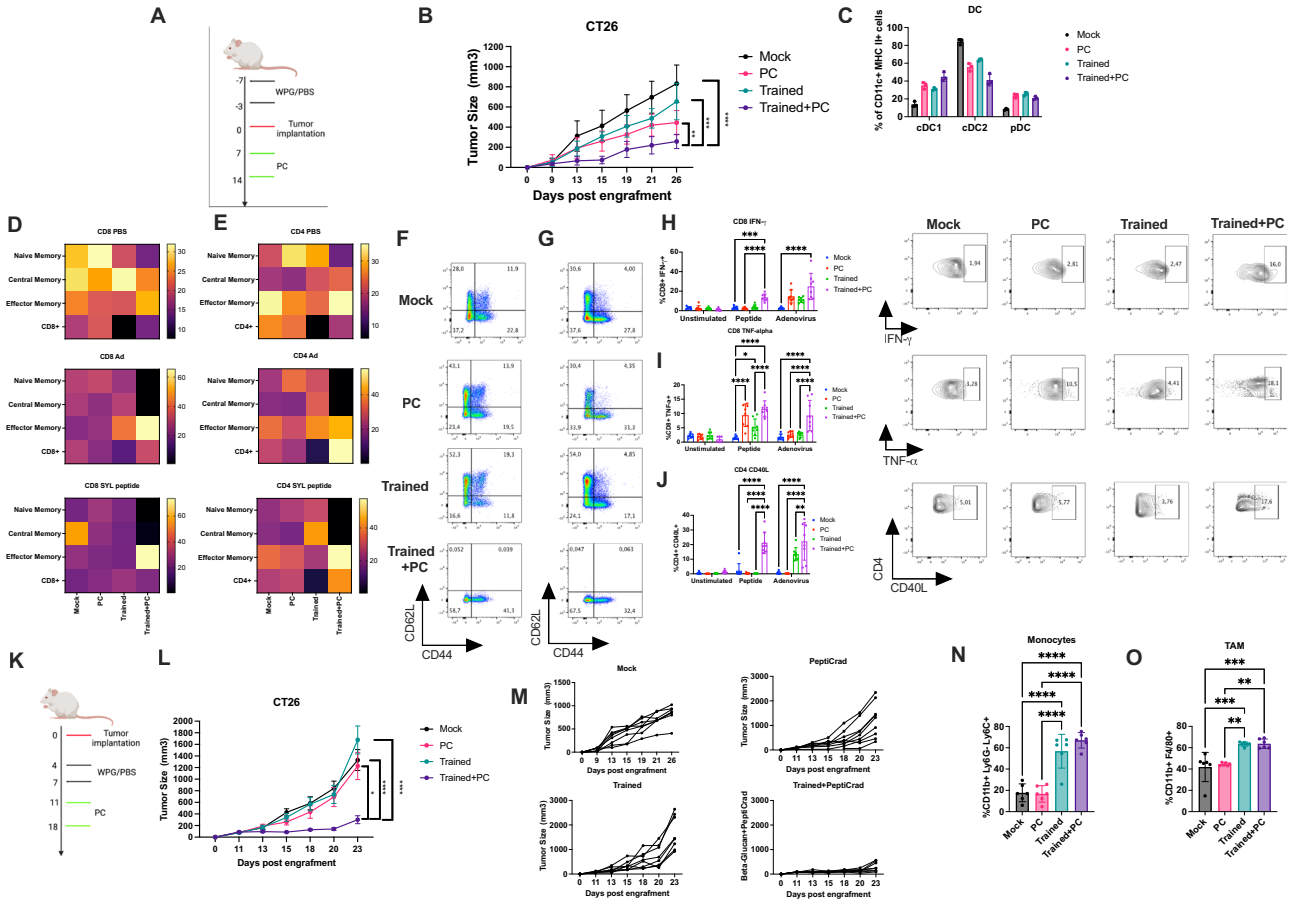

Fig. 2 | WPG-induced trained immunity enhances vaccine responses in prophylactic and therapeutic CT26 models. A Schematic of dosing schedule for CT26 tumor–bearing mice (Created in BioRender. Hamdan, F. (https://BioRender.com/i5tffm5). **B** Tumor growth curves from $n = 8$ mice per group (PC, $p = 0.0013$; Trained, $p = 0.0002$; Mock, $p < 0.0001$), analyzed by two-way ANOVA. **C** Quantification of dendritic cell subsets in draining lymph nodes pooled from $n = 8$ mice per group (technical replicates $n = 3$): cDC1 and cDC2. **D** Heat map of CD8$^+$ T cell memory subsets from splenocytes stimulated with PBS, Ad5/3 (Ad), or Syl peptide ($n = 3$ mice per group). **E** Heat map of CD4$^+$ T cell memory subsets from splenocytes stimulated with PBS, Ad5/3, or Syl peptide (n = 8 mice per group). **F–G** Representative flow cytometry dot plots of CD8$^+$ (**F**) and CD4$^+$ (**G**) T cell memory subsets after Syl peptide stimulation in Trained+PC mice. **H** IFN-γ production by CD8$^+$ T cells following stimulation with media, Syl peptide (Peptide; "***" $p = 0.0003$; "****" $p < 0.0001$), or Ad5/3 ((Adenovirus; "****" $p < 0.0001$) obtained from $n = 8$ mice per group. **I** TNF-α production by CD8$^+$ T cells after stimulation with media, Syl peptide Peptide; ("*" $p = 0.023$; "****" $p < 0.0001$), or Ad5/3 (Adenovirus; "****" $p < 0.0001$); $n = 8$ mice per group. **J** CD40L expression in CD4$^+$ T cells after media, Syl peptide (Peptide; "****" $p < 0.0001$), or Ad5/3 (Adenovirus; "**" $p = 0.026$; "****", $p < 0.0001$); $n = 8$ mice per group. **K** Therapeutic dosing schedule in CT26-bearing mice (Created in BioRender. Hamdan, F. (2025) https://BioRender.com/g9bsknf). **L** Summary of tumor size from $n = 8$ mice per group. **M** Individual tumor growth traces for each mouse. **N** Monocyte infiltration in the TME at day 25 ("****" $p < 0.0001$). O Macrophage infiltration in the TME ($n = 6$ per group; PC vs Trained+PC, $p = 0.0010$; PC vs Trained, $p = 0.0012$, Mock vs Trained +PC, $p = 0.0003$, Mock vs Trained, $p = 0.003$). Statistical significance was assessed with two-way ANOVA for the tumor growth along with a Šídák's multiple comparisons test. One-way ANOVA was used for all flow cytometry analyses along with a Tukey's multiple comparisons test. All data are presented as the mean ± SD. Schematics for experiments were created using Biorender.com. Source data are provided as a Source Data file.

analysis revealed pronounced increases in multiple amino acids (alanine, serine, glutamic acid, valine, asparagine, malic acid, arginine), fatty acids, and key intermediates of the creatine pathway (creatine, creatine phosphate, creatinine) (Fig. 3C, and Supplementary Fig. 7B–C). Differential metabolite analysis confirmed the upregulation of several amino acids and creatinine (Fig. 3D, and Supplementary Fig. 7D). Pathway impact analysis further identified upregulation of amino acid biosynthesis (notably arginine, serine, glutamic acid), fatty acid synthesis, and pathways linked to aerobic glycolysis and the Warburg effect, supported by elevated lactate (Fig. 3E). Metabolite set enrichment analysis reinforced these findings, showing enrichment of glycolytic, amino acid, and lipid pathways (Fig. 3F). Collectively, these data suggest Trained+PC promotes a coordinated shift toward biosynthetic and energy-generating programs. Given these findings, we sought to explore how different metabolic pathways were interconnected (Supplementary Fig. 7D). Correlation analysis revealed strong associations between nucleotide biosynthesis, amino acid metabolism, fatty acid synthesis, and the Warburg effect. To visualize the relationships among these metabolic pathways, we constructed a network-based metabolite interaction map (Supplementary Fig. 7E). This analysis revealed a clear interconnection between amino acid metabolism, fatty acid biosynthesis, and nucleotide synthesis, further supporting our hypothesis that Trained+PC treatment induces a coordinated metabolic shift towards biosynthetic and energy-generating pathways.

To functionally validate these observations, we performed Seahorse extracellular flux assays on isolated murine macrophages, due to their high abundance in the tumor (Fig. 2J). Following 18 h of ex vivo stimulation with PBS or WPG, trained macrophages exhibited significantly higher oxygen consumption rates (OCR) across two plating densities (40k and 80k cells) (Fig. 3H), with increases in basal and maximal respiration (Supplementary Fig. 8A–C). Notably, a major part

https://doi.org/10.1038/s41467-026-68466-5

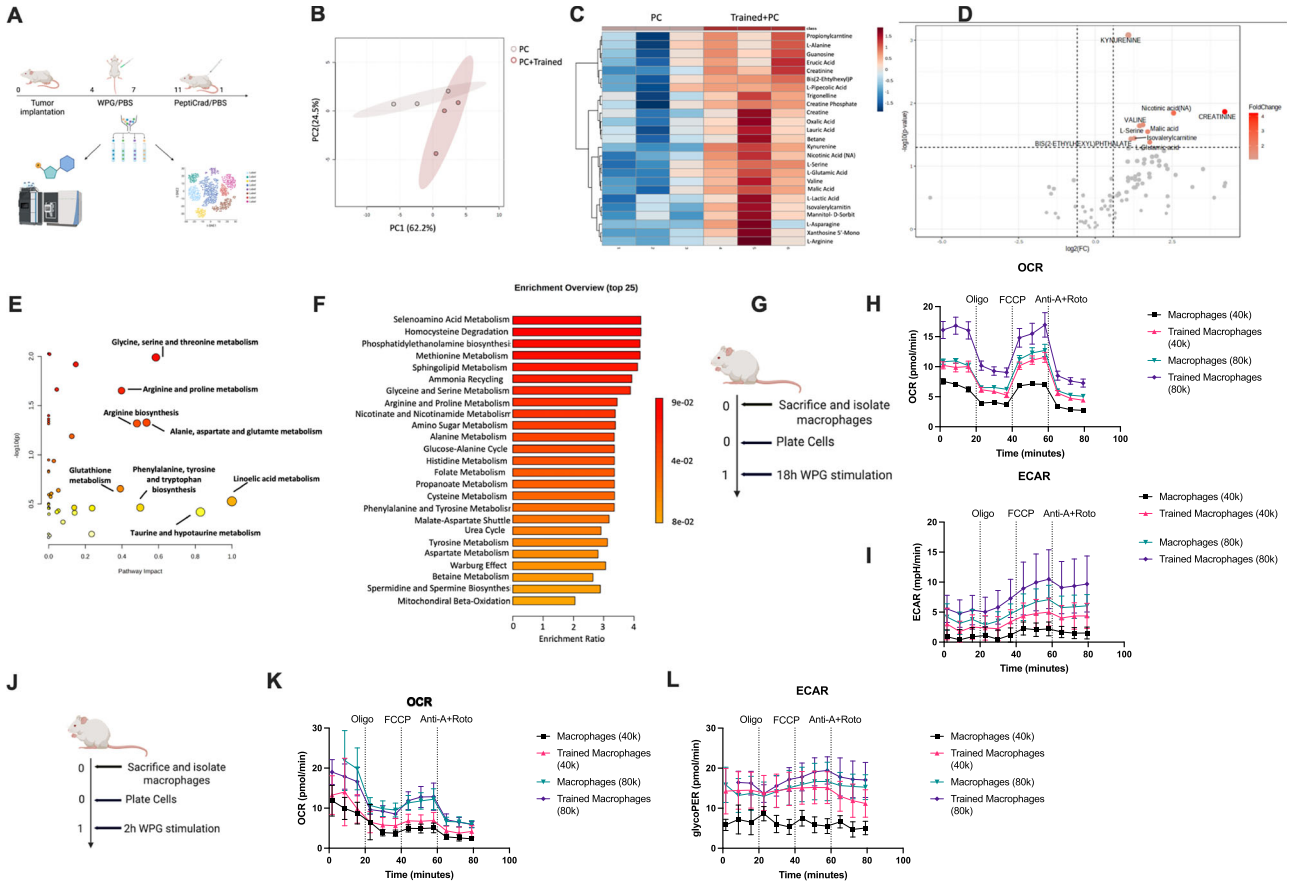

Fig. 3 | Metabolomics analysis reveals trained immune cells display Warburg metabolism and high creatine metabolism. A Workflow of post-analysis done to mice treated with PC and WPG in a therapeutic setting (Created in BioRender. Hamdan, F. (https://BioRender.com/j8s7y9l). At day 25, CD11b cells from the tumor microenvironment of PC and Trained+PC mice were sorted and both metabolomics and single RNA sequencing data was performed. **B** Principal component analysis of PC and Trained+PC mice groups based on the metabolomic signature obtained from $n = 3$ mice from each treatment group. **C** Heat-map distribution of 25 most significant metabolites in Trained+PC treated mice compared to PC treated mice. **D** Differential metabolite analysis on upregulated metabolites from Trained+PC treated mice compared to PC treated mice. P-values were calculated using a two-sided t-test and adjusted for multiple comparisons using FDR **E** Pathway impact analysis on upregulated metabolites from Trained+PC treated mice. Pathway significance was assessed using a two-sided hypergeometric test; topology was based on relative-betweenness centrality. **F** Top 25 metabolic enriched pathways in Trained+PC treated mice. **G** Graphical representation of workflow of animal experiment (Created in BioRender. Hamdan, F. (https://BioRender.com/ux8avhz). Mice were sacrificed and macrophages were enriched from spleens. Cells were plated at two different cell concentrations (40,000 and 80,000 cells) overnight. Macrophages were then stimulated with WPG for 18 h **H** OCR analysis macrophages treated with PBS or WPG for 18 h **I** ECAR analysis macrophages treated with PBS or WPG for 18 h obtained from $n = 7$ for each treatment group. **J** Graphical representation of workflow of animal experiment (Created in BioRender. Hamdan, F. (https://BioRender.com/ux8avhz). Mice were sacrificed and macrophages were enriched from spleens. Cells were plated at two different cell concentrations (40,000 and 80,000 cells) overnight. Macrophages were then stimulated with WPG for 2 h **K** OCR analysis macrophages treated with PBS or WPG for 2 h **L** ECAR analysis macrophages treated with PBS or WPG for 2 h obtained from $n = 7$ for each treatment group. Graphical representation of workflow of animal experiment. Statistical significance was assessed with one-way ANOVA for the flow cytometry analysis. All data are presented as the mean ± SD. Source data are provided as a Source Data file.

of the basal OCR was attributable to non-mitochondrial oxygen consumption (Supplementary Fig. 8D). In parallel, trained macrophages displayed elevated extracellular acidification rates (ECAR), with higher levels both at basal conditions and after inhibition of the mitochondrial ATP synthesis, consistent with an augmented glycolytic activity (Fig. 3I) and basal glycolysis levels (Supplementary Fig. 8D).

To probe the kinetics of this metabolic rewiring, we repeated the assay after only 2 h of stimulation. Under these conditions, OCR remained comparable between groups (Fig. 3K; and Supplementary Fig. 8F–H). Again, most OCR reflected non-mitochondrial oxygen consumption (Supplementary Fig. 8I). Yet, ECAR was already significantly increased in trained macrophages (Fig. 3L), accompanied by elevated basal glycolysis (Supplementary Fig. 8J). These results demonstrate that WPG rapidly reprograms macrophages toward glycolysis, consistent with a Warburg-like phenotype that is established within hours and further reinforced over time

Together, metabolomic and bioenergetic profiling converge to show that trained macrophages undergo broad metabolic rewiring characterized by enhanced amino acid and lipid biosynthesis, creatine metabolism, and a pronounced shift toward aerobic glycolysis. This reprogramming provides the energy and biosynthetic capacity required to sustain pro-inflammatory and anti-tumor functions in the context of vaccination.

Single-cell RNA sequencing reveals a distinct innate immune landscape following trained + PC therapy

To assess how Trained+PC alters the innate immune landscape in tumors, we performed scRNA-seq on sorted CD11b+ cells from tumor-bearing mice treated with PC or Trained+PC. This allowed us to capture treatment-driven changes across the myeloid compartment. Clustering revealed diverse innate populations, with macrophages, monocytes, and NK cells as dominant subsets (Fig. 4A,

https://doi.org/10.1038/s41467-026-68466-5

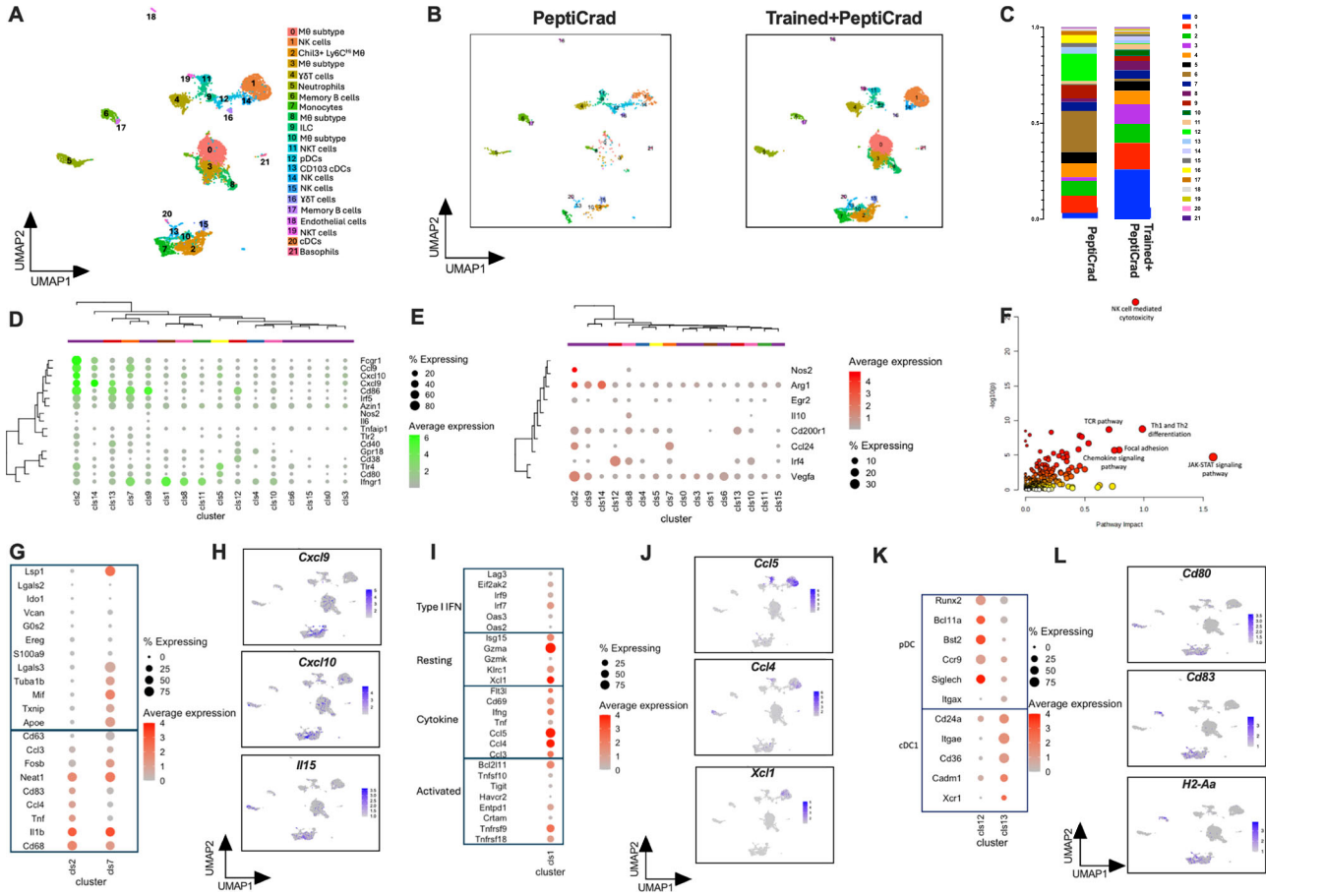

Fig. 4 | Single-cell RNA sequencing reveals an activation shift in Chil3+ Ly6C^{High} macrophages leading to NK and cDC1 infiltration. A Single-RNA sequencing data from sorted CD11b cells from the tumor microenvironment of PC and Trained+PC groups obtained from *n* = *3* mice from each treatment group. Two dimensional UMAP representation of 7814 cells from the two treatment groups aggregated together. **B** Deconvolution of UMAP dimensions from PC (1251 cells) and Trained +PC (6563 cells) groups. **C** Relative frequency of cells in each cluster across samples displayed in a bar graph. **D** Dot plot of 17 DEG activation genes across all clusters in the Trained+PC group **E** Dot plot of 8 DEG inhbitory genes across all clusters in the Trained+PC group**. F** Joint analysis of single cell RNA sequencing and metabolomic data from Trained+PC group. Pathway impact was assesed based on DEG and upregualted metabolites. Significance was assessed using a two-sided hypergeometric test with FDR correction. **G** Dot plots on activation and inhibitory genes of clusters 2 and 7 of Trained+PC group. **H** UMAP of sinlge cell RNA sequencing data showing *Cxcl9*, *Cxcl10* and *Il15* expression in all clusters of Trained +PC group. **I** Dot plots on certain genes to phenotype clusters 1 of Trained+PC group. **J** UMAP of sinlge cell RNA sequencing data showing *Ccl5*, *Ccl4* and *Xcl1* expression in all clusters of Trained+PC group. **K** Dot plots on certain genes to phenotype clusters 12 and 13 of Trained+PC group. **L** UMAP of sinlge cell RNA sequencing data showing *Cd80*, *Cd83* and *H2-Aa* expression in all clusters of Trained+PC group. Statistical significance was assessed with one-way ANOVA for the flow cytometry analysis. Schematics for experiments were created using Biorender.com. Source data are provided as a Source Data file.

and Supplementary Figure 9 A). Clusters 0, 3, 2, 7, 10, and 1 (macrophages, monocytes, NK cells) were significantly expanded in Trained+PC, demonstrating remodeling of the TME (Fig. 4B, C). Consistent with this, Trained+PC upregulated cytokines such as *cxcl9* and *cxcl2* (Supplementary Fig. 9B), suggesting enhanced recruitment of T and NK cells. Analysis did reveal a clear expression of *itgam* (CD11b) on majority of clusters (Supplementary Fig. 9C), with minimal contamination, demonstrating successful enrichment.

We next sought to identify the functional programs within these clusters. Stratification revealed two major inflammatory patterns (Fig. 4D). First, clusters 2 (*chil3+ ly6Chi* macrophages, Supplementary Fig. 9D), 14 (NK), 13 (cDC1), 7 (monocytes), and 9 (ILCs) upregulated *fcgr1*, *ccl9*, *cxcl9/10*, *cd86*, and *irf5*, consistent with a pro-inflammatory phenotype. Expression of *lyz2* and *tnfaip2* in these clusters (Supplementary Fig. 9E) further supported myeloid-driven inflammation, with cluster 2 showing the strongest response. Second, clusters 1 (NK), 8 (monocytes), and 11 (NKT) displayed a type I IFN signature (Ifngr1). We also examined β-glucan sensing and found *clec7a* (dectin-1), a key receptor involved in β-glucan recognition[41,42], broadly expressed in inflammatory clusters (Supplementary Fig. 9F), except NK/NKT cells, suggesting indirect NK activation via cytokines and chemokine crosstalk within the tumor microenvironment.To test whether Trained+PC shifted cells toward suppression, we analyzed anti-inflammatory genes. Few were detected (Fig. 4E): cluster 2 macrophages showed limited *nos2/arg1* expression, but this was confined to a minority. Thus, Trained+PC promoted durable inflammatory activation rather than compensatory suppression.

To further dissect a mechanism of action, we performed a joint-pathway enrichment analysis, integrating scRNA-seq data with previously obtained metabolomic screening (Fig. 4F). Notably, pathways associated with T cell activation, including TCR signaling and Th1/Th2 differentiation, were significantly enriched, suggesting that Trained +PC therapy enhanced adaptive immune priming. Additionally, chemokine signaling and JAK-STAT pathways emerged as key regulatory networks, indicating that cytokine-driven immune modulation was a central feature of the treatment-induced changes. Interestingly, NK cell-mediated cytotoxicity was among the most significantly upregulated pathways, despite NK cells themselves not expressing dectin-1. This strongly suggests that their expansion and activation were

secondary to inflammatory cues from other myeloid populations rather than direct WPG signaling.

To dissect the mechanisms driving NK cell expansion, we analyzed monocyte and macrophage clusters, as these cells are primary producers of cytokines known to recruit and activate NK cells (Fig. 4G). Cluster 2 macrophages exhibited a markedly heightened inflammatory profile compared to cluster 7 monocytes, suggesting a dominant role in orchestrating the immune response. Expression analysis confirmed that cluster 2 macrophages strongly upregulated *cxcl9*, *cxcl10*, and *il15*—key factors known to drive NK cell recruitment, proliferation, and cytotoxicity (Fig. 4H). These findings imply that trained immunity-induced macrophages (Chil3+ Ly6Chi macrophages) act as central regulators of NK cell expansion and function within the tumor microenvironment.

Given the substantial NK cell infiltration observed in Trained+PC-treated tumors, we further characterized cluster 1 NK cells to define their functional phenotype (Fig. 4I), based on previous classification methods[45]. By classifying these cells into resting, cytokine-responsive, activated, and type I IFN-responsive subpopulations, we observed a predominant enrichment of cytokine-responsive NK cells (Fig. 4I). This was accompanied by robust upregulation of chemokines such as *ccl5, ccl4*, and *xcl1* (Fig. 4J), which are known to facilitate the recruitment of conventional dendritic cells (cDCs). Moreover, among the top genes with the principal component analysis was *ccl5* (Supplementary Fig. 9G) further demonstrating its importance. Hence, the chemokine-producing NK phenotype suggests a critical role for NK cells in shaping subsequent antigen-presenting cell (APC) activation. Moreover, cluster 1 NK cells from Trained+PC treated mice were seen to have similar levels of *pdcd1, tigit, havcr2* indicating no exhaustion effects (Supplementary Fig. 10A). This was further confirmed when analysing the NK cells from the tumor microenvironment of mice trained after tumor implantation (Supplementary Fig. 10B).

To examine the downstream impact on APC function, we analyzed clusters 12 and 13, representing plasmacytoid dendritic cells (pDCs) and conventional dendritic cells (cDC1), respectively (Fig. 4K). cDC1s (cluster 13) showed marked upregulation of antigen-presentation genes *cd80*, *cd83*, and *h2-Aa* (Fig. 4K, L), consistent with an activated phenotype. Thus, Trained+PC did not merely expand cDC1s but enhanced their functional capacity.

Together, these experiments reveal a possible sequential activation cascade: trained macrophages (cluster 2) secrete Cxcl9/10 and Il15, recruiting NK cells; NK cells secrete Ccl5/Xcl1, enhancing cDC1 infiltration and activation; cDC1s then prime T cells. This macrophage–NK–cDC1 axis could provide a mechanistic explanation for the superior efficacy of Trained+PC compared to PC alone.

Creatine Regulation in Trained Immunity Enhances Pro-Inflammatory Cytokine Release and NK cell infiltration

To dissect the metabolic requirements of trained immunity, we enriched splenic CD11b$^+$ cells, exposed them to PBS or WPG, and restimulated them with adenovirus in the presence or absence of metabolic inhibitors targeting glycolysis/mTOR (rapamycin), HIF-1α stabilization (ascorbate), or creatine uptake (β-GPA) (Fig. 5A). PBS-treated cells produced no TNF-α, whereas WPG-trained cells showed robust TNF-α and IL-6 induction, both of which were significantly reduced by inhibitors (Fig. 5A, B). Since our scRNA-seq data highlighted CXCL9 and CXCL10 as key chemokines strongly upregulated in trained macrophages, we next assessed their secretion. Consistent with our single-cell findings, trained CD11b$^+$ cells secreted significantly higher levels of CXCL9 and CXCL10 compared to PBS controls. However, secretion was abolished when rapamycin, ascorbate, or β-GPA were added, demonstrating that both glycolytic and creatine-dependent metabolism support the pro-inflammatory reprogramming of trained macrophages.

Since the initial experiments tested inhibitor effects only during secondary stimuation, we repeated the assays by adding inhibitors during the *priming stage* of WPG training. As expected, trained cells produced elevated IL-6, TNF-α, CXCL9, and CXCL10 upon adenovirus stimulation, yet this was severely blunted by all inhibitors when given at priming (Supplementary Fig. 11A–E). Moreover, when we washed β-GPA and supplemented with creatine, CXCL9 and CXCL10 expressions were rescued (Supplementary Fig. 11D and E). To directly test whether creatine metabolism impacts epigenetic programming or only effector function, we focused on macrophages, as they emerged in our single-cell analysis as the key trained population driving the NK–cDC1 axis. CD11b$^+$F4/80$^+$ macrophages were therefore enriched and stained for H3K4me3, a histone mark associated with trained immunity. Compared to PBS controls, WPG-trained macrophages showed a marked increase in H3K4me3 after adenovirus stimulation (Supplementary Fig. 11F). This enrichment was preserved even in the presence of β-GPA (Supplementary Fig. 11G), indicating that creatine does not influence the acquisition of trained epigenetic marks but rather sustains effector function during secondary challenge. We next assessed whether WPG-induced epigenetic remodeling regulates expression of the creatine transporter Slc6a8. ChIP-qPCR for H3K4me3 showed no enrichment at the *Slc6a8* locus (Supplementary Fig. 11H). However, RT-qPCR revealed a significant increase in *Slc6a8* transcript levels in trained macrophages compared to PBS-treated controls (Supplementary Fig. 11I), suggesting that upregulation of creatine transport occurs independently of H3K4me3-mediated epigenetic induction.

To assess the role of creatine in adaptive immunity induced by PC, we tested whether β-GPA treatment affected tumor control. CT26-bearing mice were treated with PBS or WPG (trained) and vaccinated with PC, with a subset receiving daily β-GPA to block creatine uptake (Fig. 5C). As expected, Trained+PC provided the strongest tumor control (Fig. 5D, and Supplementary Fig. 12A). In contrast, β-GPA treatment partially impaired this effect, with tumors growing larger than in Trained+PC but remaining smaller than in mock controls (Fig. 5C, D, and Supplementary Fig. 12A). β-GPA alone did not affect tumor growth, confirming it has no intrinsic anti- or pro-tumor activity.

To dissect immune alterations, we analyzed tumor infiltration of macrophages and NK cells (Supplementary Fig. 11B). Macrophage numbers were unchanged between Trained+PC and Trained+PC+β-GPA groups (Fig. 5E and F), whereas NK cell infiltration was markedly reduced in β-GPA–treated tumors (Figures G and H). This aligns with our earlier finding that β-GPA suppresses CXCL9/CXCL10 secretion from trained CD11b$^+$ cells, chemokines critical for NK recruitment.

To evaluate epigenetic remodeling in vivo, we stained tumor-derived CD11b$^+$F4/80$^+$ macrophages. Trained+PC increased H3K4me3 compared to PBS controls (Fig. 5I, J). Importantly, this enrichment persisted despite β-GPA, reinforcing that creatine does not drive epigenetic programming but instead supports effector responses. Together, these results demonstrate that creatine metabolism is a central driver of the effector phase of trained immunity in CRC, sustaining cytokine and chemokine production (including CXCL9 and CXCL10) and enabling NK cell recruitment, without altering the underlying epigenetic reprogramming.

Macrophage-NK cell crosstalk promotes DC infiltration and CD8 + T cell memory in trained immunity

To clarify the functional roles of macrophages and NK cells in trained immunity–mediated tumor control, we selectively depleted these subsets in CT26-bearing mice prior to WPG training and PC vaccination (Fig. 6A). Flow cytometry confirmed efficient depletion (Supplementary Fig. 13A). Tumor growth showed that loss of either subset impaired control, while dual depletion abolished efficacy (Fig. 6B, Supplementary Fig. 13B), demonstrating non-redundant, complementary roles.

https://doi.org/10.1038/s41467-026-68466-5

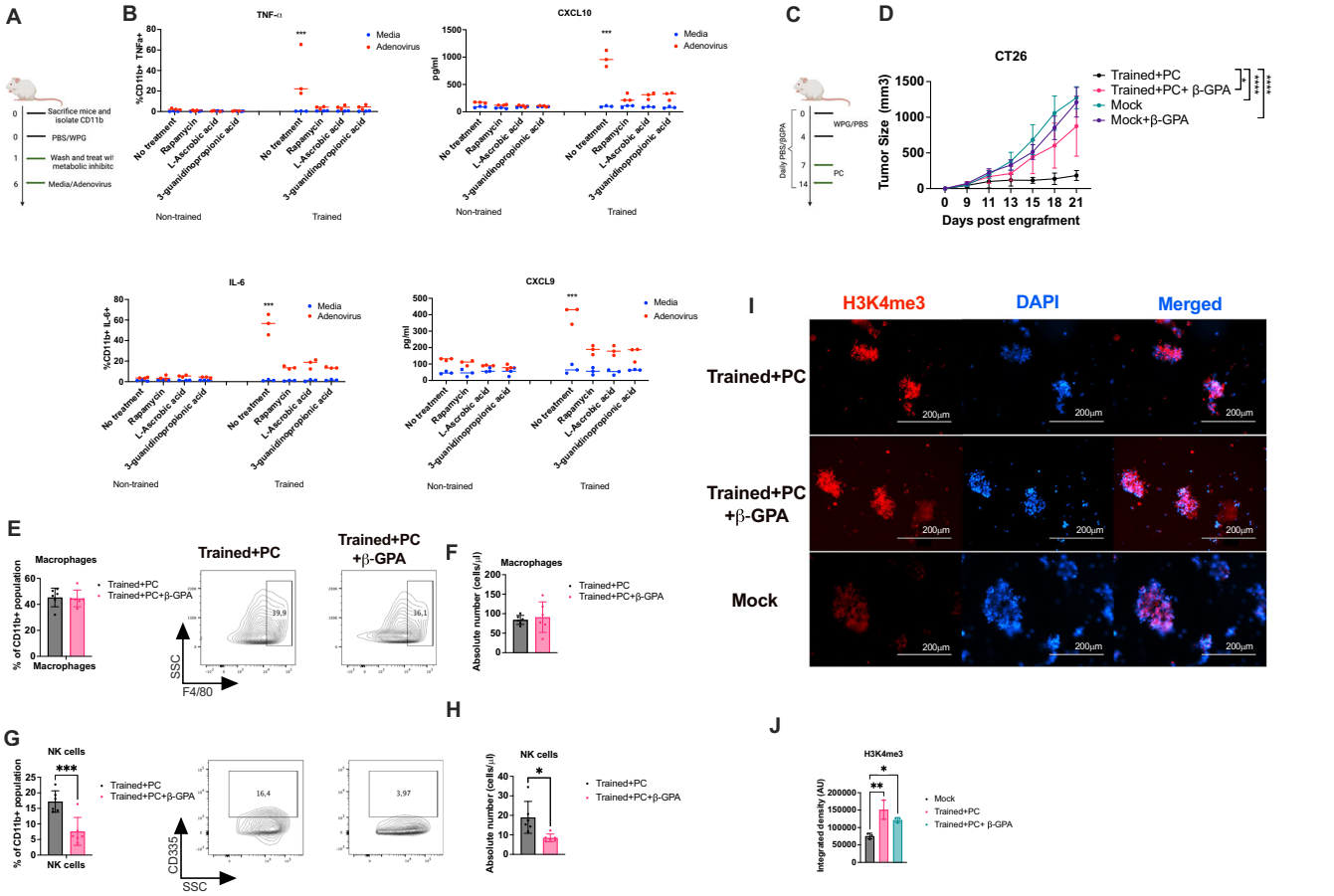

Fig. 5 | Creatine aids trained macrophages but meeting high energy requirements for chemokine expression. A Schematic of workflow of metabolic inhibition of trained immunity (Created in BioRender. Hamdan, F. (https://BioRender.com/16b56c0). **B** Quantification of TNF-α ("***" $p = 0.0003$), IL6 ("***" $p = 0.0003$), CXCL9 ("***" $p = 0.0001$)and CXCL10 ("***" $p = 0.0002$) from non-trained and trained cells treated with different metabolic inhibitors and stimulated with media or adenovirus obtained from $n = 3$ mice from each treatment group.s. **C** Graphical representation of mouse experiment blocking creatine (Created in BioRender. Hamdan, F. (https://BioRender.com/3nxhps2). Balb/C mice were injected subcutaneously with CT26 and then given daily injections of β-GPA. **D** Tumor sizes were measured for each group every 2-3 days and summarized. For Trained+PC and Trained+PC + β-GPA data points were obtained from $n = 8$ mice, while for Mock and Mock + β-GPA obtained from $n = 5$ mice. ("*" p = 0.0263; "****" $p < 0.0001$) **E** Quantification of macrophages in the tumor microenvironments at day 23 obtained from $n = 6$ mice from each treatment group. Contour plots of macrophage populations in the tumor microenvironments. **F** Absolute numbers of macrophages in the tumor microenvironments across each group obtained from $n = 6$ mice from each treatment group. **G** Quantification of NK cells in the tumor microenvironments at day 23. Contour plots of macrophage populations in the tumor microenvironments obtained from $n = 6$ mice from each treatment group ("**" $p = 0.002$) **H** Absolute numbers of NK cells in the tumor microenvironments across each group obtained from $n = 6$ mice from each treatment group. ("**" $p = 0.012$) **I** Immunofluorescence staining of CD11b + F4/80+ enriched macrophages for trained immunity marker, H3K4me3, and DAPI across groups at day 23 obtained from $n = 3$ mice from each treatment group (scale bars of 200μm). **J** Image intensity analysis of H3K4me3 signal across each group. Statistical significance was assessed with two-way ANOVA for the tumor growth along with a Šídák's multiple comparisons test. For the flow cytometry and H3K4me3 density analysis, a one-way ANOVA test was performed along with a Tukey's multiple comparisons test. For metabolic inhibition studies, a two-way ANOVA test was performed along with a Tukey's multiple comparisons test. All data are presented as the mean ± SD. Source data are provided as a Source Data file.

We next asked how these cells influence systemic immunity. Splenocytes from Trained+PC mice contained abundant EM CD8 + T and CM CD8 + T cells after Syl peptide restimulation (Fig. 6C), whereas depletion of macrophages or NK cells reduced both populations (Fig. 6D). This correlated with impaired DC recruitment, particularly cDC1, as shown by flow cytometry (Supplementary Fig. 14A, B). Functionally, $CD8^+$ T cell cytokine production (IFN-γ, TNF-α) was strongly reduced in depleted groups (Supplementary Fig. 14C, D). Together, these results indicated that macrophages and NK cells together form a critical upstream axis necessary to establish effective adaptive immunity. To further define the role of T cells, we repeated the experiments in CT26-bearing mice treated with Trained +PC but depleted of $CD8^+$ T cells (Supplementary Fig. 15A). Successful depletion was confirmed by blood analysis (Supplementary Fig. 15B), and we observed that these mice completely lost tumor control (Supplementary Fig. 15C). Thus, trained macrophages or NK cells alone are insufficient to mediate tumor control in the absence of $CD8^+$ T cells.

To dissect this relationship further, we performed adoptive transfer experiments with PBS- or WPG-treated macrophages and NK cells into CT26-bearing mice that were subsequently vaccinated with PC (Fig. 6E, Supplementary Fig. 16A and B). Remarkably, only mice receiving trained macrophages in combination with PC exhibited significant tumor growth reduction (Fig. 6F). Transfer of trained NK cells alone did not affect tumor burden, establishing macrophages as the primary initiating population in this circuit. Consistently, trained macrophage transfer led to higher frequencies of splenic EM CD8 + T cells (Fig. 6G) and enhanced cytokine responses upon antigen restimulation, with significantly elevated IFN-γ and TNF-α production in CD8 + T cells (Fig. 6H, I).

Analysis of the tumor microenvironment further supported this hierarchy. Mice receiving trained macrophages plus PC displayed

https://doi.org/10.1038/s41467-026-68466-5

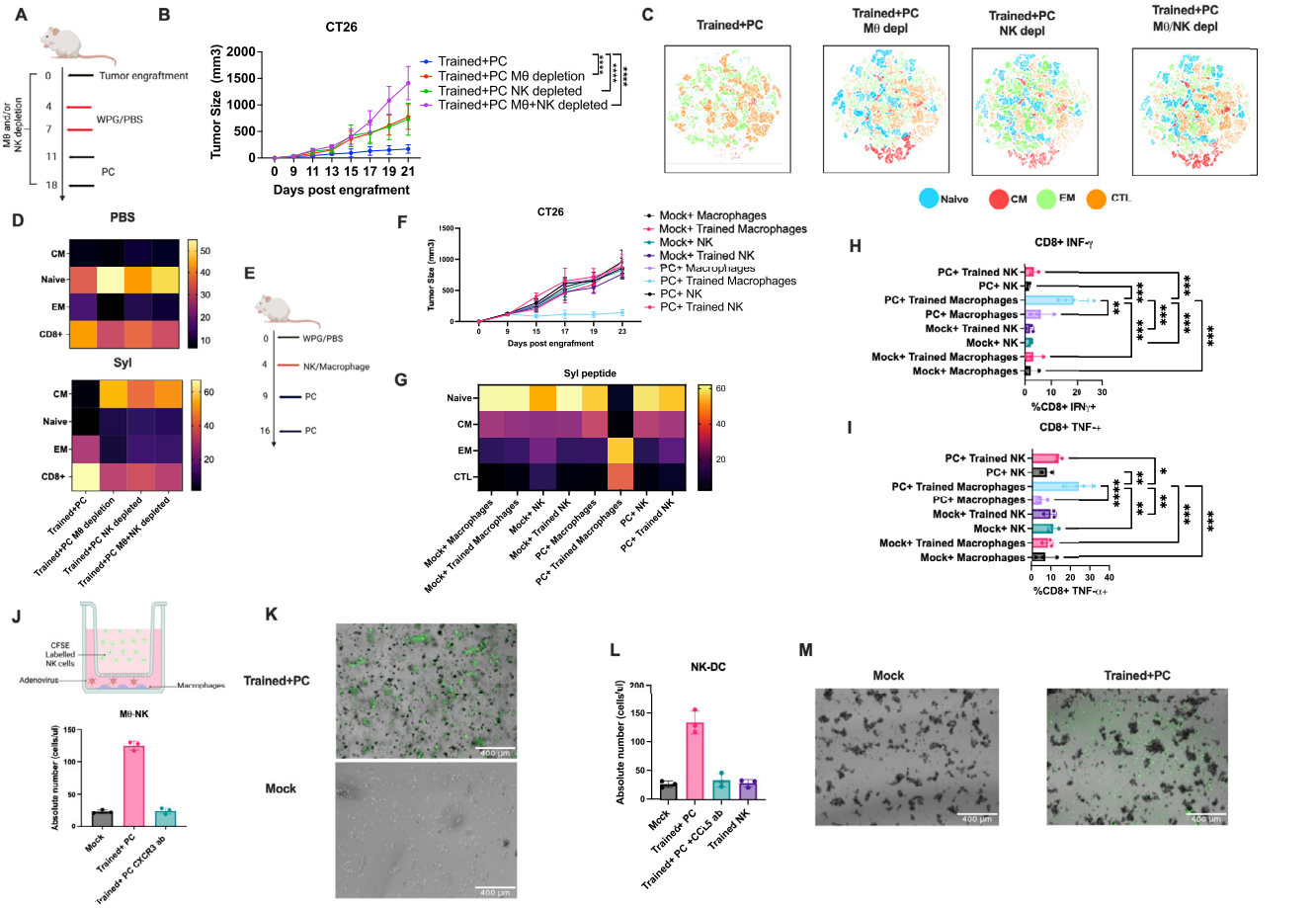

Fig. 6 | Macrophages and NK cells are required for trained immunity to enhance vaccine efficacy. A Dosing scheme for macrophage and NK cell depletion in CT26-bearing mice (Created in BioRender. Hamdan, F. (https://BioRender.com/sckv9it). **B** Tumor sizes from n = 8 mice per group ("****" $p < 0.0001$). **C** UMAP projection of $CD8^+$ splenocytes at day 23 ($n = 3$ per group). **D** Heat maps showing $CD8^+$ T-cell memory subsets stimulated with PBS or Syl peptide ($n = 6$ per group). **E** Dosing scheme for macrophage and NK adoptive transfer (Created in BioRender. Hamdan, F. (https://BioRender.com/knbij2y). **F** Tumor sizes from $n = 5$ mice per group. **G** Heat maps of $CD8^+$ T-cell memory subsets stimulated with Syl peptide ($n = 3$ per group). **H** Quantification of IFN-γ^+ $CD8^+$ splenocytes after Syl stimulation at day 23 ($n = 3$ per group) (PC + Trained Macrophages vs. Mock + Macrophages $p = 0.0001$; vs. Mock + Trained Macrophages $p = 0.0003$; vs. Mock + NK p = 0.0001; vs. Mock + Trained NK $p = 0.0001$; vs. PC + Macrophages $p = 0.0021$; vs. PC + NK p = 0.0003; vs. PC + Trained NK $p = 0.0003$). **I** Quantification of TNF-α^+ $CD8^+$ splenocytes after Syl stimulation at day 23 ($n = 3$ per group) (PC + Trained Macrophages vs. Mock + Macrophages $p = 0.0003$; vs. Mock + Trained Macrophages $p = 0.0006$; vs. Mock + NK p = 0.0031; vs. Mock + Trained NK $p = 0.0014$; vs. PC + Macrophages $p < 0.0001$; vs. PC + NK $p = 0.0015$; vs. PC + Trained NK p = 0.0190). **J** Schematic of NK chemotaxis transwell assay (Created in BioRender. Hamdan, F. (https://BioRender.com/8yxqt1n): CFSE-labeled NK cells placed in the upper chamber migrated toward macrophages stimulated with Ad5/3; NK cells were treated with 10 μg/mL anti-CXCR3 antibody ($n = 3$ technical replicates). **K** Confocal images of CFSE-labeled NK cells migrating toward macrophages. **L** DC chemotaxis assay in which NK cells stimulated with Ad5/3 were treated with 10 μg/mL anti-CCL5 antibody ($n = 3$ technical replicates). **M** Confocal images of CFSE-labeled DCs migrating toward NK cells. Statistical significance was assessed with two-way ANOVA for tumor growth along with a Šídák's multiple comparisons test. A one-way ANOVA for flow cytometry and cell migration analyses along with a Tukey's multiple comparisons test. All data are presented as the mean ± SD. Source data are provided as a Source Data file.

increased intratumoral macrophages (Supplementary Fig. 17A) and NK cells (Supplementary Fig. 17B). Importantly, these NK cells were functionally activated, as demonstrated by increased perforin expression (Supplementary Fig. 17C). While no changes were detected in plasmacytoid DCs (pDCs; Supplementary Fig. 17D) or cDC2 populations (Supplementary Fig. 17E–F), cDC1 tumor infiltration was markedly increased in the trained macrophage + PC group (Supplementary Fig. 17G). This increase coincided with the expansion of EM CD8 + T cells in the TME (Supplementary Fig. 17H), reinforcing the link between macrophage-driven NK cell recruitment, subsequent cDC1 activation, and effective T cell priming.

To directly assess the crosstalk between macrophages and NK cells, we employed a transwell migration assay in which CFSE-labeled NK cells were placed in the upper chamber and macrophages isolated from Trained+PC or mock tumors were placed below. NK cells showed greater migration toward Trained+PC-derived macrophages compared to controls (Fig. 6J, K). Microscopy confirmed this enhanced recruitment. Importantly, pre-treatment of NK cells with a CXCR3-blocking antibody markedly reduced migration, demonstrating that macrophages recruit NK cells via the CXCL9/CXCL10–CXCR3 axis.

We next asked whether NK cells could, in turn, recruit dendritic cells (DCs). Using the same transwell system, NK cells isolated from the TME of Trained+PC-treated mice, but not from mock tumors, promoted DC migration (Fig. 6L, M). This effect was abrogated by CCL5 blockade, implicating NK cell–derived CCL5 in DC recruitment (Fig. 6L). FLT3L blockade did not affect DC recruitment, further highlighting the need of CCL5 (Supplementary Fig. 18A). Notably, mock NK cells treated with WPG in vitro did not increase DC migration, suggesting that NK cell functional activation requires signals present within the trained TME rather than direct β-glucan exposure.

To investigate the transcriptional basis of these observations, we performed ChIP-qPCR on macrophages isolated from PBS- or WPG-treated mice. Trained macrophages displayed elevated H3K4me3 enrichment at *cxcl9* and *cxcl10* loci (Supplementary Fig. 18B), consistent with epigenetic rewiring driving sustained chemokine production. In contrast, NK cells from either PBS- or WPG-treated mice did not show H3K4me3 enrichment at *ccl5, ccl4*, or *flt3* loci (Supplementary Fig. 18C). Similarly, NK cells isolated from the TME of Trained+PC mice lacked detectable epigenetic marks at these genes. However, RT-qPCR of whole-cell lysates revealed that NK cells from Trained+PC tumors did express increased levels of *ccl5* mRNA (Supplementary Fig. 18D). These results suggest that NK cells are not epigenetically rewired by trained immunity but are instead secondarily activated within the TME, likely through macrophage-derived cues.

Because creatine metabolism sustained macrophage CXCL9/10 output, we asked whether it also maintains the macrophage–NK–cDC1 axis. Adoptive transfer of trained macrophages plus PC vaccination was combined with β-GPA treatment (Supplementary Fig. 19A). β-GPA impaired tumor control (Supplementary Fig. 19B) and reduced NK infiltration (Supplementary Fig. 19D) without affecting macrophage numbers (Supplementary Fig. 19C).

To determine whether creatine metabolism itself was epigenetically imprinted, we performed ChIP-qPCR for H3K4me3 at the creatine transporter gene *slc6a8*. No enrichment was detected in trained macrophages (Supplementary Fig. 119E), yet RT-qPCR of cell lysates revealed increased *slc6a8* expression (Supplementary Fig. 19F). Thus, trained macrophages acquire enhanced creatine reliance, but this metabolic adaptation is transcriptional rather than epigenetic.

Together, these experiments establish that trained macrophages are the initiating population, epigenetically rewired to secrete CXCL9/10, which recruit NK cells via CXCR3. NK cells then amplify immunity by producing CCL5, driving cDC1 infiltration and T cell priming. Creatine metabolism sustains this axis by maintaining macrophage chemokine output, highlighting a hierarchical, metabolically supported macrophage–NK–cDC1–T cell circuit critical for anti-tumor efficacy.

Trained immunity enhances vaccine efficacy in the MC38 and colon-26 tumor model

To determine whether the effects of trained immunity extended beyond the CT26 model, we next tested the MC38 colorectal cancer model. Mice were depleted of macrophages and/or NK cells before PBS or WPG training and peptide vaccination (Fig. 7A). Trained+PC treatment produced superior tumor control, with many mice achieving complete clearance (Fig. 7B, and Supplementary Fig. 20A). Depletion of either subset partially impaired protection, while combined depletion abolished it, mirroring CT26 results.

We then evaluated adaptive immunity. Splenic profiling showed marked expansion of EM and CM $CD8^+$ T cells in Trained+PC mice (Fig. 7C, D, and Supplementary Fig. 20B), together with elevated IFN-γ and TNF-α after peptide stimulation (Fig. 7E, F, and Supplementary Fig. 20C, D). These responses were lost with macrophage or NK depletion. In draining lymph nodes, Trained+PC mice displayed increased cDC1 frequencies, consistent with enhanced cross-presentation, whereas depletion shifted the balance toward cDC2 dominance (Fig. 7G, and Supplementary Fig. 20E).

Because creatine metabolism sustained chemokine production in earlier experiments, we asked whether it also regulated Trained+PC efficacy in vivo. Mice received β-GPA to block creatine uptake (Fig. 7H). While Trained+PC again provided robust control, β-GPA treatment partially reversed protection (Fig. 7I, and Supplementary Fig. 20F), reducing EM/CM $CD8^+$ T cells (Fig. 7J), IFN-γ and TNF-α production (Fig. 7K, L), and cDC1 accumulation in draining lymph nodes (Fig. 7N). These results confirm that creatine metabolism is required for NK- and DC-dependent amplification of trained immunity.

Finally, to validate findings in a more immunosuppressive context, we used the Colon-26 model, which is APC-mutant, refractory to PD-1/PD-L1 therapy, and considered more clinically relevant to human CRC (Supplementary Fig. 21A). Vaccination alone failed to control tumors, whereas Trained+PC significantly suppressed growth (Supplementary Fig. 21B, C). Trained+PC tumors showed increased macrophage infiltration (Supplementary Fig. 21D), greater NK accumulation (Supplementary Fig. 21E), and enhanced cDC1 recruitment in draining lymph nodes (Supplementary Fig. 21F). Splenocytes from Trained+PC mice produced higher IFN-γ and IL-2 upon A1H5 peptide restimulation (Supplementary Fig. 21H–I) and exhibited increased EM $CD8^+$ T cells (Supplementary Fig. 21J).

Together, these results demonstrate that the macrophage–NK–cDC1 axis drives vaccine efficacy not only in CT26 but also in MC38 and the highly immunosuppressive Colon-26 model. Trained immunity consistently promoted cDC1 recruitment, robust effector and memory $CD8^+$ T cell responses, and dependence on creatine metabolism, supporting its potential as a broadly applicable enhancer of CRC vaccination.

Trained Immunity Enhances Vaccine Responses and Tumor Killing in CRC Patient Derived Organoids

To extend our preclinical findings to human settings, we first examined the clinical significance of macrophage subsets using publicly available datasets. In a cohort of 163 patients with CRC (cBioPortal), stratification by CD206 expression—a marker typically associated with M2-like macrophages—revealed that patients with high CD206 expression had significantly longer disease-free survival compared to those with low expression (Fig. 8A). Further stratification of the CD206-high cohort (n = 123) based on CXCL9 expression demonstrated that individuals with elevated CXCL9 levels displayed superior outcomes (Fig. 8B). These results suggest that macrophages acquiring a $CXCL9^+$ phenotype may promote improved anti-tumor immunity, consistent with the macrophage–NK–cDC1 axis we identified in our murine models.

We next sought to determine whether WPG-induced trained immunity could be recapitulated in human immune cells and whether it could augment vaccine responses. PBMCs and monocytes from healthy donors were trained with WPG for 24 h, washed, and subsequently stimulated with adenovirus, the adjuvant used in the PC vaccine. While non-trained monocytes produced modest IL-6 and TNF-α responses, trained monocytes exhibited markedly higher cytokine frequencies and concentrations following adenovirus stimulation (Supplementary Fig. 22 A). Differentiation of trained monocytes into macrophages or dendritic cells retained these effects: trained macrophages produced significantly higher IL-6 and TNF-α levels, while trained DCs exhibited increased IFN-γ secretion and elevated expression of CD83, a costimulatory molecule critical for T cell priming (Supplementary Fig. 22B–C). These findings indicate that trained immunity enhances the responsiveness of the myeloid compartment to adenoviral stimulation, potentially amplifying downstream vaccine effects.

We then evaluated whether trained PBMCs could enhance antigen-specific T cell responses to a clinically tested HLA-A2–restricted CEA peptide vaccine. PBMCs from $HLA\text{-}A2^+$ donors were treated with PBS or WPG, stimulated with peptide, and restimulated on day 6 (Fig. 8C). Across three independent donors, trained PBMCs exhibited enhanced IFN-γ responses compared to PBS controls (Fig. 8D–E), confirming that trained immunity augments vaccine-induced T cell activation in a human context.

To assess functional relevance against tumors, we tested trained PBMCs in co-culture with CRC patient-derived organoids (PDOs). PBMCs from $HLA\text{-}A2^+$ donors were trained with WPG and expanded with CEA peptide, followed by $CD8^+$ T cell enrichment and co-culture with PDOs (Fig. 8F). After 24 h, microscopy and Z-stack imaging revealed increased PI staining of tumor cells in PDO#2 and PDO#3

https://doi.org/10.1038/s41467-026-68466-5

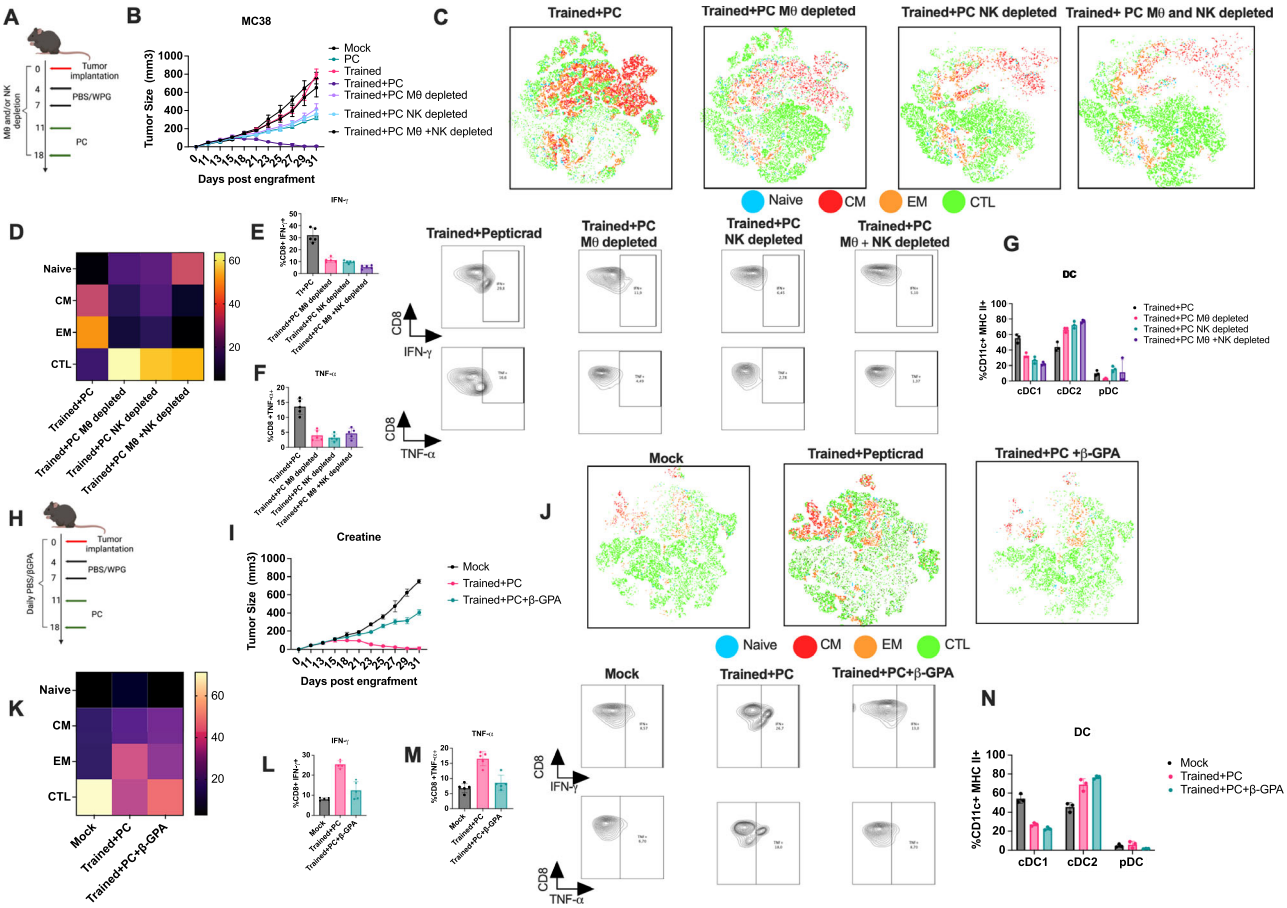

Fig. 7 | Trained immunity enhances vaccine responses in MC38 tumor models. **A** Treatment schedule for MC38-bearing mice (Created in BioRender. Hamdan, F. (https://BioRender.com/3c0jk7s). **B** Tumor sizes from $n = 5$ mice per group. C UMAP projection of CD8⁺ splenocytes at day 33 after MC38 peptide stimulation ($n = 5$ per group). **D** Heat map quantifying CD8⁺ T-cell responses after MC38 peptide stimulation ($n = 5$ per group). **E** Quantification of IFN-γ–producing CD8⁺ splenocytes stimulated with MC38 peptides at day 33 ($n = 5$ per group). **F** Quantification of TNF-α–producing CD8⁺ splenocytes stimulated with PBS or Syl peptides at day 33 ($n = 5$ per group). **G** Analysis of dendritic cell subsets from draining lymph nodes at day 33; lymph nodes from $n = 5$ mice per group were pooled and each data point represents a technical replicate ($n = 3$). **H** Treatment schedule for a second MC38 tumor experiment (Created in BioRender. Hamdan, F. (https://BioRender.com/3nxhps2). **I** Tumor sizes from $n = 5$ mice per group. **J** UMAP projection of CD8⁺ splenocytes at day 33 after MC38 peptide stimulation ($n = 5$ per group). **K** Heat map quantifying CD8⁺ T-cell responses after MC38 peptide stimulation ($n = 5$ per group). **L** Quantification of IFN-γ–producing CD8⁺ splenocytes at day 33 ($n = 5$ per group). **M** Quantification of TNF-α–producing CD8⁺ splenocytes stimulated with PBS or Syl peptides at day 33 ($n = 5$ per group). **N** Draining lymph node dendritic cell analysis at day 33; lymph nodes from $n = 5$ mice were pooled and each data point represents a technical replicate ($n = 3$). Statistical significance was assessed using two-way ANOVA for tumor growth along with a Šídák's multiple comparisons test. A one-way ANOVA for flow cytometry analyses along with a Tukey's multiple comparisons test. All data are presented as the mean ± SD. Source data are provided in the Source Data file.

when cultured with trained PBMCs compared to non-trained controls (Fig. 8G, H, and Supplementary Fig. 23A). LDH cytotoxicity assays confirmed enhanced tumor cell killing across multiple PDOs (Fig. 8I). Importantly, macrophages trained with WPG did not exhibit any direct tumoricidal activity when co-cultured with PDOs (Supplementary Fig. 23B), suggesting that their role is indirect, mediated through orchestration of NK and T cell responses.

To directly test whether macrophages are essential for trained immunity in human settings, we first examined their metabolic and epigenetic changes. Compared to PBS controls, WPG-trained macrophages showed higher glucose uptake (Supplementary Fig. 23C), indicating metabolic activation. ChIP-qPCR further revealed increased H3K4me3 enrichment at the *Cxcl9* and *Cxcl10* loci (Supplementary Fig. 23D), demonstrating that trained macrophages undergo epigenetic remodeling to boost chemokine expression. Functionally, trained macrophages promoted NK cell migration in a transwell assay dependent on the CXCR3 axis, consistent with their role in initiating the NK–cDC1 axis (Supplementary Fig. 23E).

We next tested whether macrophages are required for boosting vaccine-induced responses. PBMCs from HLA-A2⁺ donors were either left intact or depleted of monocytes/macrophages before WPG training. Both groups were then stimulated with a clinically tested CEA peptide vaccine and tested in a killing assay against HCT116 CRC cells. Intact PBMCs trained with WPG exhibited significantly enhanced tumor killing compared to non-trained controls (Supplementary Fig. 23F). In contrast, PBMCs lacking monocytes/macrophages failed to show any increase in tumor killing after WPG training, even when the vaccine peptide was provided (Supplementary Fig. 23F). This demonstrates that macrophages are indispensable for trained immunity in humans: they provide the initial reprogramming signal that enables NK cell recruitment, DC activation, and ultimately stronger CD8⁺ T cell–mediated tumor killing.

Discussion

Advancing cancer vaccines in colorectal cancer (CRC), particularly for tumors with a lower mutational burden, demands a deeper understanding of the crosstalk among various components of the tumor microenvironment (TME) in response to vaccination. In this study, we integrated publicly available data on a pancreatic cancer model[40], single-cell RNAseq (scRNAseq), flow cytometry and metabolomics data

https://doi.org/10.1038/s41467-026-68466-5

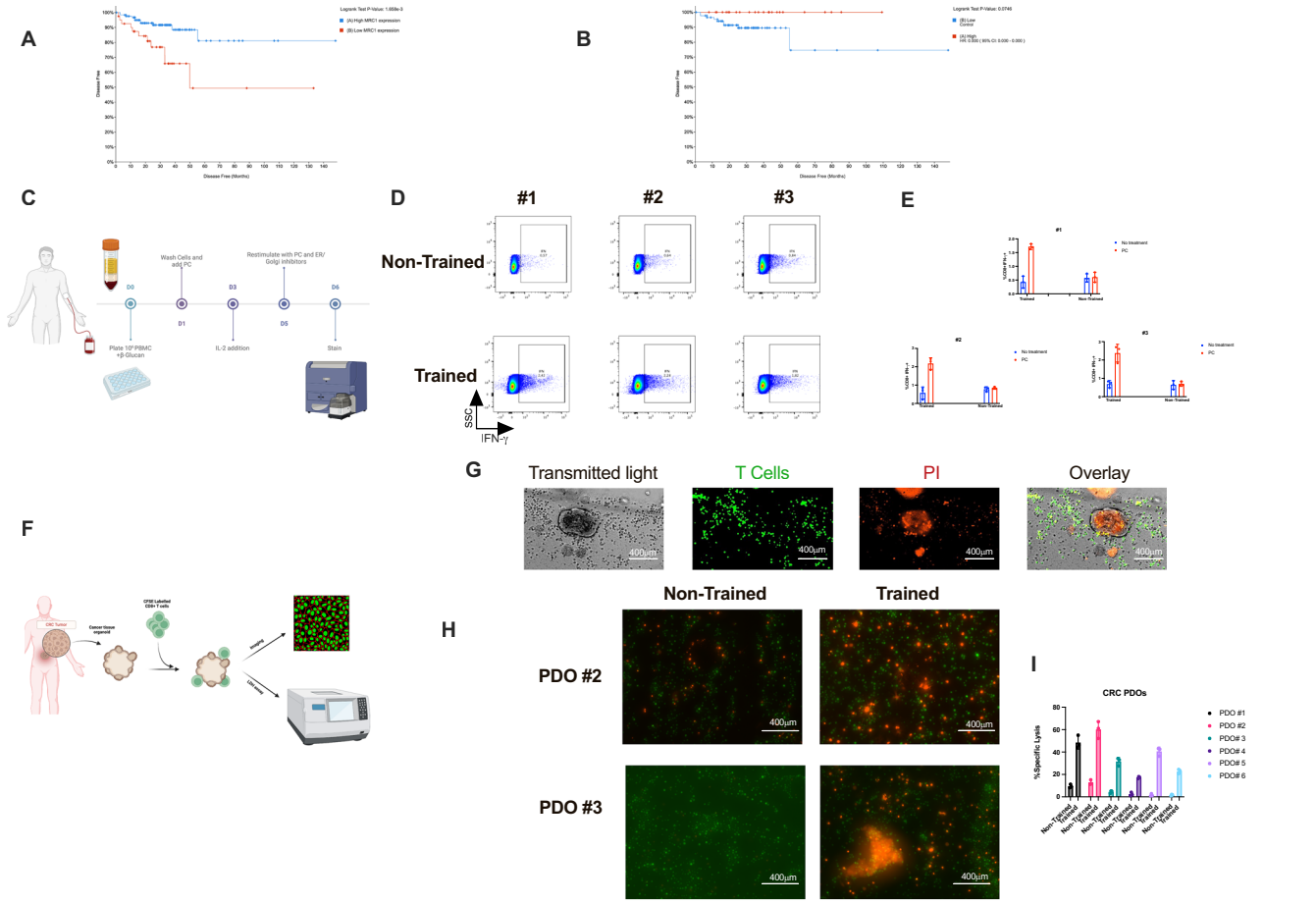

Fig. 8 | Trained immunity can enhance vaccine effects with human PBMCs and PDOs. A Disease free survival of CD206^{High} ($n = 123$) and CD206^{Low} ($n = 40$) expression in 163 colorectal cancer patient. **B** From the 123 CD206^{High} patients, patients were divided in CXCL9^{High} ($n = 25$) and CXCL9^{Low} ($n = 98$) and disease-free survival was calculated. **C** Schematic of workflow for training human PBMCs and vaccinating. HLA-A2 buffy coats were obtained and PBMCs were collected. 10^6 PBMCs were plated per well and treated with WPG for one day and then washed with PBS. PC against CRC peptides were added and cells were stimulated with IL-2 at day 3. At day 5, cells were restimulated with PC and stained (Created in BioRender. Hamdan, F. (https://BioRender.com/wro2gql). **D** Flow-cytometry plots of CD8 + T cells expressing IFN-γ from each treatment group when stimulated with PC against CRC peptides obtained from $n = 3$ technical repeats from each healthy donor. **E** Quantification of CD8 + T cells expressing IFN-γ across treatment groups when stimulated with PC against CRC peptides obtained from $n = 3$ technical repeats from each healthy donor. **F** Schematic of workflow of organoid culture and T cell killing. CRC tumor samples were obtained from patients and grew as organoids. Expanded PBMCs against CRC peptides were enriched for CD8 + T cells and labeled with CellTracker™ Green and co-cultured with PDOs. Killing was observed under a microscope and performing an LDH assay (Created in BioRender. Hamdan, F. (https://BioRender.com/9hnhrpy). **G** Confocal images of T-cell killing of PDO obtained from patient #1. Killing was analysed by PI staining. **H** Z-stalks of confocal images for T-cell killing of PDO obtained from patient #2 and #3. **I** Quantification of specific lysis, from LDH release, from each patient across treatment groups obtained from $n = 3$ technical repeats for each CRC PDO. All data are presented as the mean ± SD. Schematics for experiments were created using Biorender.com. Source data are provided as a Source Data file.

on our in vivo model of CRC, followed by validation on a different in vivo model and PDOs to dissect the role of trained immunity in enhancing the efficacy of PC vaccination. A key finding was that WPG exposure plays a pivotal role in the metabolic and epigenetic adaptation of immune cells, particularly macrophages, allowing an enhanced pro-inflammatory cytokine secretion. This adaptation facilitates the recruitment and activation of other immune cells, such as NK cells and cDC1 cells, establishing a robust anti-tumor T-cell response. Previous studies have provided compelling evidence supporting the use of trained immunity in cancer[37–40]. For example, Kalafati and colleagues showed that β-glucan-induced training enhances myeloid cell activation and tumor infiltration, leading to significant tumor suppression[38]. Moreover, BCG-induced trained immunity has been shown to reprogram innate immune cells to overcome immunosuppressive barriers. More recently, Wattenberg and colleagues reported that co-activation of myeloid receptors like CD40 and Dectin-1 synergistically boosts trained immunity, resulting in improved T cell-mediated tumor control[39]. Together, these findings underscore the therapeutic potential of leveraging trained immunity to elicit durable anti-tumor responses and provide a strong rationale for integrating this strategy into CRC immunotherapy.

Our re-analysis of publicly available data from Geller and colleagues[40] supports the notion that WPG treatment induces sustained myeloid reprogramming, reinforcing trained immunity mechanisms in their pancreatic cancer model. The progressive accumulation of Chil3 + Ly6C+ macrophages and monocytes over time suggests a lasting imprint on the innate immune compartment, supported by an enhanced expression of the antigen presentation machinery, as well as activation of the adaptive immunity. Consistent with this, in their cancer vaccine model, WPG-pretreated mice displayed significant alterations in T cell memory subsets, with a shift from central to effector memory CD8 + T cells. Furthermore, these trained mice exhibited heightened IFN-γ and TNF-α production upon antigenic stimulation, underscoring an enhanced functional response.

These findings suggest that WPG-mediated trained immunity not only remodels the myeloid landscape but also drives a more robust and durable T cell response, aligning with the broader implications of innate-adaptive crosstalk in anti-tumor immunity.

An increase in cDC1, monocytes and macrophages were observed in mice treated solely with WPG yet this did not have a substantial anti-tumor effect with our colon cancer models. Wattenberg and colleagues also showed a similar trend where mice trained with the BCG vaccine displayed a similar tumor control to mock mice with pancreatic cancer implanted subcutaneously[39]. Only when mice trained with BCG and treated with anti-CD40 antibodies did a superior tumor control was observed. This may indicate that subcutaneous engrafted tumors specific may need further immune activation might be required to gain an effective anti-response from trained immunity.

The NK-macrophage-cDC1 axis has emerged as a key component of effective anti-tumor immunity in multiple tumor models[46,47]. Macrophages have been shown to be key in orchestrating effective anti-tumor responses. A recent study showed that disrupting CD206+ macrophages led to a decreased NK infiltration which in response reduced cDC1 infiltration[48]. Similar to our results, they demonstrated CXCL9 as a key chemokine expressed by CD206+ macrophages in recruiting NK cells. Human patients having an intact macrophage-NK-cDC1 axis were shown to have a better survival compared to patients whose axis was disrupted. In CRC, these macrophages are often skewed toward immunosuppressive phenotypes[49–56], impairing effective immune activation and possibly recruitment of the NK-cDC1 axis. By reprogramming macrophages through trained immunity, we can potentially restore this axis, enabling enhanced tumor antigen presentation, cytokine secretion, and subsequent T cell priming (Supplementary Fig. 24).

Our scRNA-seq analysis revealed that Chil3+Ly6C^{high} macrophages were the primary cell population driving the NK-cDC1 axis. This is surprising given that these macrophages are typically classified as regulatory or pro-tumoral cells, often associated with wound healing and immune suppression in the TME[57–59]. However, under trained immunity conditions, these macrophages displayed a phenotype more aligned with pro-inflammatory and anti-tumor functions, suggesting that their role in the immune response may be more plastic than previously thought. One possible explanation for this shift is that trained immunity reprograms these macrophages to adopt a hybrid phenotype, retaining some regulatory functions while acquiring the ability to produce pro-inflammatory cytokines. Another possibility is that the increased presence of IFN-γ in the trained environment altered the macrophage polarization state, pushing Chil3+ Ly6C^{high} macrophages toward an M1-like phenotype capable of supporting anti-tumor activity.

A key hallmark of trained immunity is the metabolic rewiring that underpins long-term functional changes in innate immune cells. Our metabolomic analysis revealed significant shifts in central metabolic pathways, particularly in amino acid metabolism and energy production. These changes align with previous studies showing that trained macrophages undergo a shift toward glycolysis, pentose phosphate pathway activation, and cholesterol biosynthesis, all of which support increased cytokine production and inflammatory activity[60]. Interestingly, our data revealed a significant increase in creatine metabolism, a finding that has not been extensively explored in the context of trained immunity. Creatine is traditionally associated with muscle energy metabolism, but recent evidence suggests it plays an important role in immune cell activation by buffering ATP levels. This has been demonstrated with macrophages and T cells, where creatine supplementation enhanced anti-tumor activity[61]. Given that trained macrophages require a large ATP supply to sustain cytokine and chemokine synthesis, we hypothesize that creatine metabolism is essential for fueling the high metabolic demands of trained immunity. Specifically, macrophages may rely on creatine to support the expression of key inflammatory chemokines such as CXCL9 and CXCL10, which are crucial for T cell and NK cell recruitment. This finding suggests that creatine metabolism may be an overlooked yet essential component of myeloid cell activation and could represent a potential target for enhancing trained immunity-based therapies.

Our findings show that trained immunity can enhance vaccine efficacy in CRC by reprogramming myeloid cells to sustain long-term immune activation. The clinical relevance of this approach is supported by the use of PDOs, which provide a highly predictive model for patient-specific responses to immunotherapy. Additionally, the use of a clinically tested CEA peptide vaccine highlights the translational potential of our strategy, as CEA is a well-established tumor antigen with ongoing trials in multiple cancer types[62]. From a broader perspective, these findings have implications for the development of next-generation cancer vaccines. By integrating trained immunity with established immunotherapy approaches, we may be able to overcome the limitations of current vaccines and checkpoint inhibitors, particularly in tumors resistant to traditional T cell-mediated approaches. Ultimately, our study provides a strong rationale for further exploration of trained immunity in cancer immunotherapy, specifically cancer vaccine therapy. Given its ability to reprogram the innate immune system for sustained anti-tumor activity, trained immunity-based approaches could represent a paradigm shift in cancer treatment, offering hope for patients with cancer vaccine-resistant malignancies.

While our study provides evidence for the role of trained immunity in enhancing colorectal cancer vaccination, several limitations should be acknowledged. First, our in vivo models, though robust, may not fully recapitulate the complexity and heterogeneity of human CRC, and further validation in diverse patient cohorts, including patient-derived models, is required to strengthen translational relevance. Second, while we delineated the metabolic and epigenetic mechanisms underpinning β-glucan–induced training, we did not assess how long these functional changes persist. Our functional assays demonstrate efficacy several weeks after training, yet dedicated longitudinal experiments—such as late tumor inoculation, immune rechallenge, and serial profiling of trained macrophages—will be critical to define persistence and memory-like features in cancer contexts. Finally, as with all preclinical studies, translation to the clinic will require not only mechanistic validation in human immune subsets but also evaluation of safety, dosing, and combinatorial regimens with existing therapies.

Methods

Ethical permits

The iCAN Flagship Project biobank study is based on a biobank consent and was reviewed by the HUS Ethical Committee and is executed based on a HUS research permit (4.5.2023 §38 (HUS/223/2023), a Findata data permit (THL/1338/14.02.00/2022), and MTAs with Helsinki Biobank (HBP20210170) and Finnish Hematology and Registry Biobank FHRB (12.5.2022).

All animal studies were evaluated and authorized by the Experimental Animal Committee of the University of Helsinki and the Provincial Government of Southern Finland (permits ESAVI/11895/2019 and ESAVI/12722/2022). Our ethical authorization limits tumor size to a maximum diameter of 18 mm, and this limit was not exceeded in any experiment conducted for this study.

Murine cell lines

Murine colon adenocarcinoma CT26 (ATCC Cat# CRL-2638) was purchased from the American Type Culture Collection (ATCC) after 2013. Murine colon adenocarcinoma MC38 (Kindly provided by Cristian Smerdou, Cima Universidad de Navarra). Murine colon adenocarcinoma Colon-2 was purchased from Cytion (Product number: 400156). Cell lines were thawed at passage 5 and kept in culture until reaching passage 15. All cell lines were authenticated by the ATCC, cultured

under appropriate conditions and regularly checked for mycoplasma contamination.

Preparation of conditionally replicating adenovirus

All adenoviruses were generated as conditionally replicating adenoviruses using standard protocols previously described[40,63]. In short, adenovirus viruses are of the chimeric 5/3 serotype with a 24-nucleotide deletion and deleteion of the gp19k region in the E1A region resulting in selective replication in Rb-deficient pathway cells.

PC complex formation

The PeptiCab complex was generated by combining the adenoviral vector with a peptide that includes a polyK tail. Twenty micrograms of PolyK-extended epitopes were incubated with the 1×10^9 viral particles for 15 minutes at room temperature prior to treatment with the resulting complexes. Detailed information on the stability and formation of the complex has been reported previously[41,42]. The specific quantities of peptide and virus used in each experiment are provided in the corresponding figure legends.

PBMCs, PMNs and monocyte collection

Polymorphonuclear cells (PMNs) and peripheral blood mononuclear cells (PBMCs) were isolated from buffy coats as previously described[65]. The PBMC and PMN layers were subsequently removed between serum and Ficoll (Cytivia, Cat# 1714400) or in the Histopaque (Sigma-Aldrich, Cat# 11191) layer, respectively, and cultured in 1xRPMI (Roswell Park Memorial Institute, Gibco, Cat# 21875034),

PBMC were processed for monocyte enrichment using density gradient centrifugation with Percoll(Sigma-Aldrich,Cat# P1644) solutions. PBMC suspension (containing approximately $150-200 \times 10^6$ cells) was carefully layered onto a hyper-osmotic Percoll. Tubes were centrifuged at 580 g for 15 min and cells at the interface were collected and then centrifuged at 350 g for 7 min. Cell pellet resuspended in RPMI medium to produce a monocyte-enriched suspension. To further purify the monocyte population by removing platelets and dead cells, 10 mL of iso-osmotic Percoll solution was overlaid with 3 mL of the monocyte-enriched suspension (up to 200×10^6 cells) followed by centrifugation at 350 g for 15 min. The supernatant was removed, and cell pellets were resuspended in RPMI medium. Samples were taken from buffy coats from the Finnish Red Cross blood service (ethical permit 26/2025).

Tumor implantation and innate immune training for animal experiments

All animal experiments were reviewed and approved by the Experimental Animal Committee of the University of Helsinki and the Provincial Government of Southern Finland (license number ESAVI/11895/2019). Around 4–6-week-old immunocompetent female BALB/c mice, purchased from Envigo (Venray, Netherlands), injected in the right flank with 500,000 CT26 cells. As for MC38 tumors, C57BL/6 mice purchased from Envigo (Venray, Netherlands) were injected in the right flank with 500,000 cells. All mice were maintained on a standard rodent chow diet provided ad libitum. Animals received dry pellet feed (Envigo; Catalog No. 2018S) unless otherwise specified. Food and water were always available throughout the experiments. Tumor volume was calculated using the following formula:

$$Tumor\ Volume = \frac{long\ measure \times (short\ measure)^2}{2}$$

A complete randomization was performed on the day of the treatment. Details on the schedule of the treatment can be found in the figure legends. The viral dose used was 1 × 109 vp/tumor complexed with 20 μg of a single peptide. The tumors were measured with a caliper and the mice were sacrificed when the humane ethical endpoint was met.

For prophylactic settings, mice were trained by injecting two I.P administrators of 1 mg of WPG (Invivogen, Cat# tlrl-wgp) 7 and 4 days before tumor implantation. For therapeutic settings, mice were first implanted with tumors and then at day 4 and 7 post-tumor implantation were injected with two administering of 1 mg of WPG (Invivogen, Cat# tlrl-wgp) I.P.

For adoptive transfer experiments, macrophages and NK cells were isolated from splenocytes of donor mice. $CD11b^+$ cells were first enriched using CD11b magnetic beads (BioLegend, 480109, 5 μl/1 million cells of biotin, 10 μl/1 million cells of nanobeads) and further purified into $F4/80^+$ macrophages using F4/80 magnetic beads (BioLegend, 480169, 5 μl/1 million cells of biotin, 10 μl/1 million cells of nanobeads). NK cells were enriched using a NK isolation beads (BioLegend, 480049, 5 μl/1 million cells of biotin, 10 μl/1 million cells of nanobeads). Purified macrophages or NK cells were stimulated with 1 μg/mL WPG for 24 h, washed extensively, and subsequently transferred into recipient mice (1×10^6 cells per mouse, I.P.).

In vivo depletion of specific immune cell types

For macrophage depletion, mice were administered i.p. with 200 μl of chlodronate liposomes (Liposoma, Cat# C-005) 1 day after tumor implantations and then every four days until the end of the experiment. As for NK depletion, mice were treated with 50 μl of anti-Asialo-GM1 antibodies (Purified anti-Asialo-GM1 Antibody, BioLegend, Cat # 146002) day after tumor implantations and given every four days until the end of the experiment. For depletion of both immune population, mice were treated with both treatments 1 day after tumor implanations and given every four days until the end of the experiment. For CD8 + T cell depletion, mice were given a bolus treatment of 500 μg of anti-CD8 antibody (BioXcell, Cat# #BE0061) given I.P 1 day prior the first PC treatment and was further sustained by injecting 100 μg of anti-CD8 antibody I.P every 3 days.

Seahorse metabolic assay

A Seahorse XFe96 Analyzer (Agilent) was used to determine oxygen consumption rate (OCR) and extracellular acidification rate (ECAR) in macrophages. Macrophages were enriched using F4/80 microbeads (BioLegend, Cat#480169). Purified macrophages were transferred to Seahorse XF Base medium (Agilent) supplemented with glucose (10 mM), sodium pyruvate (5 mM), and L-glutamine (5 mM) (Gibco), pH 7.4, at 37 °C. Cells were plated at either 0.5×10^5 or 0.8×10^5 cells per well onto Seahorse XF96 cell culture plates and allowed to adhere. Macrophages were then stimulated with either 1 μg/ml whole β-glucan particles (WPG; InvivoGen, Cat#tlrl-bgp) or PBS control for either 2 h (short-term stimulation) or overnight (16 h; long-term stimulation).

OCR and ECAR were measured using a standard Mito Stress Test. The following inhibitors were sequentially injected during the assay: oligomycin (1 μM), carbonyl cyanide 4-(trifluoromethoxy) phenylhydrazone (FCCP; 1 μM), and a mix of antimycin A and rotenone (1 μM each). Assay parameters were 3 min mixing, no wait, and 3 min measurement, repeated 3 times at baseline and after each injection. Following measurements protein determination was performed, and results were normalized for total protein content.

Creatine inhibition

Mice received I.P injection of β-GPA (500 mg/kg in 100 μl f PBS) (Sigma-Adlrich, Cat#G6878) 1 day after tumor implantations and given every day until the end of the experiment.

Intracellular stimulation and staining

Intracellular stimulation and staining were performed on 2×10^6 murine splenocytes incubated in a 96-well U-bottom plate with brefeldin A

(Biolegend, Cat# 420601) (1:1,000) and monensin A (Biolegend, Cat# 420701) (1:1,000) at 37 °C for 5 h. Stimulants were added at concentrations of 2 μg for peptides and 40 MOI for adenovirus. Following stimulation, samples were stored overnight at 4 °C. The cells were then centrifuged and the pellets were resuspended in murine Fc-block (BioLegend, Cat# 156613) at 4 °C for 15 minutes. Extracellular proteins were stained using the following antibodies: BV711 CD3 (BD Biosciences, #563123,0.5 μl/1 million cells), BV510 CD8 (BD Biosciences, #563068, 1 μl/1 million cells), PE-CF594 CD4 (BD Biosciences, #562285 0.5 μl/1 million cells), APC CD62L (eBioscience, #17-0621-81 0.5 μl/1 million cells), AF700 CD44 (BioLegend, #103026, 1 μl/1 million cells), and v450 CCR7 (BD Biosciences, #560805, 1 μl/1 million cells). After extracellular staining, the cells were fixed and permeabilized using a Fixation/Permeabilization kit (BD Biosciences) according to the manufacturer's instructions. Intracellular proteins were then stained with BV650 TNF-α (BioLegend, #506333, 1 μl/1 million cells), PE-Cy7 IL-2 (BioLegend, #503832, 1 μl/1 million cells), PE IFN-γ (BioLegend, #505808, 1 μl/1 million cells), and FITC IL-6 (BioLegend, #503806, 1 μl/1 million cells). Finally, the samples were acquired on a Fortessa flow cytometer (BD Biosciences) and analyzed with FlowJo software (version 10.8.2).

Flow cytometry of tumor samples

Tumors from mice were passed through a 70 μm cell strainer (Falcon) to obtain a cell suspension. One million cells were then plated in a 96 V bottom well plate (Sarstedt) and stained with the following antibodies: BV711 CD3 (clone: 145-2C11, cat: 563123, BD Biosciences, 0.5 μl/1 million cells), BV510 CD8 (clone: 53-6.7, cat: 563068, BD Biosciences, 1 μl/1 million cells), PE-CF594 CD4 (clone: RM4-5, cat: 562285, BD Biosciences, 0.5 μl/1 million cells), APC CD62L (clone: MEL-14, cat: 17-0621-81, eBioscience, 0.5 μl/1 million cells), AF700 CD44 (clone: IM7, cat: 103026, BioLegend, 1 μl/1 million cells), v450 CCR7 (clone: 4B12, cat: 560805, BD Biosciences, 1 μl/1 million cells), BV650 TNF-α (clone: MP6-XT22, cat: 506333, BioLegend, 1 μl/1 million cells), PE-Cy7 IL-2 (clone: JES6-5H4, cat: 503832, BioLegend, 1 μl/1 million cells), PE IFN-γ (clone: XMG1.2, cat: 505808, BioLegend, 1 μl/1 million cells), BV711 CD11b (clone: M1/70, cat: 101241, BioLegend, 0.5 μl/1 million cells), FITC CD11c (clone: N418, cat: 25-0114-82, eBioscience, 0.5 μl/1 million cells), PerCP/cy5.5H2-Kd (clone: AF6-88S, cat: 116516, BioLegend, 1 μl/1 million cells), PE CD103 (clone: 2E7, cat: 121406, BioLegend, 1 μl/1 million cells), APC PDCA (clone: 927, cat: 127015, BioLegend, 1 μl/1 million cells), APC anti-mouse CD3 (clone: 17A2, cat: 100236, BioLegend, 0.5 μg/1 million cells), FITC anti-mouse CD8a (clone: 53-6.7, cat: 100706, BioLegend, 1 μg/1 million cells) and PerCP/cy5.5 anti-mouse CD107a (LAMP-1) (clone: 1D4B, cat: 121625, BioLegend, 5 μl/1 million cells), All antibody mixes were incubated in a final volume of 100 μl and generally used according to their respective manufacturer instructions.

In-vitro human immune cell training and stimulation

100,000 purified monocytes were resuspended in a volume of 100 μL was dispensed into flat-bottom 96-well plates (Corning, NY, USA) and allowed to adhere to the polystyrene surface for 1 h at 37 °C. Afterward, cells were washed with pre-warmed. Monocytes were then incubated with either RPMI culture medium as a negative control or with 1 μg/mL of β-glucan at 37 °C for 24 h. After, cells were treated with brefeldin A (1:1,000) and monensin A (1:1,000) at 37 °C and stimulated with 40 MOI of adenoviruses or LPS (Invivogen, Cat#, tlrl-3pelps) (10 ng/ml) for 5 h. As for macrophages, monocytes were differentiated into M0 macrophages by supplementing RPMI media with 10% human heat-inactivated serum for five days. For DCs, monocytes were stimulated with GM-CSF (1000 U/ml) and IL-4 (800 U/ml) for 4 days. DCs and macrophages were then incubated with either RPMI culture medium as a negative control or with 1 μg/mL of β-glucan at 37 °C for 24 h. After, cells were treated with brefeldin A (1:1,000) and monensin A (1:1,000) at 37 °C and stimulated with 40 MOI of adenoviruses or LPS (Invivogen, Cat#, tlrl-3pelps) (10 ng/ml) for 5 h.

Ex-vivo metabolomic inhibiton

Balb/c mice were first trained with either PBS or WPG and then sacrificed. Spleens were isolated and were then passed through a 70 μm cell strainer (Falcon) to obtain a cell suspension. CD11b$^+$ cells were isolated using CD11b magnetic beads (BioLegend, 480109, 5 μl/1 million cells of biotin, 10 μl/1 million cells of nanobeads) and plated in dispensed into flat-bottom 96-well plates and allowed to adhere. CD11b$^+$ cells were then treated with 10 nM rapamycin (Sigma), 500 nM of ascorbic (Merck, Cat# APO456787373) and 10 mM of β-GPA for 5 days and then washed with PBS. CD11b$^+$ cells were then stimulated with PBS or 40 MOI of adenoviruses for 5 h. For TNF-α (BioLegend, 502909, 1 μl/1 million cells) and IL-6 measurement-α (BioLegend, 501112, 1 μl/1 million cells), CD11b$^+$ cells were treated with brefeldin A (1:1000) and monensin A (1:1000) to measure levels with intracellular flowcytometry. As for CXCL9 and CXCL10, the concentrations of each cytokine was determined in the cell culture supernatant by ELISA using MIG/CXCL9 (ThermoFisher,Cat#250-18-20UG) and murine CXCL10/IP-10 ELISA kit (R&D, Cat# DY466-05).

Immunofluorescence on F4/80 macrophages

Tumors from mice were passed through a 70 μm cell strainer (Falcon) to obtain a cell suspension. CD11b$^+$ cells were isolated using CD11b magnetic beads (BioLegend, 480109, 5 μl/1 million cells of biotin, 10 μl/1 million cells of nanobeads) and then further enriched for F4/80 macrophages using F4/80 beads (Biologend, 480169, 5 μl/1 million cells of biotin, 10 μl/1 million cells of nanobeads). F4/80 macrophage cells were plated on 8 well Nunc; Lab-Tek; II Chamber Slides and cultured for 4 days. Cells were fixed in 4% cold paraformaldehyde and stained with H3K4me3 antibody (1:200, Diagnode, C15410003) and DAPI (1μg/ml, Invitrogen™, P36941) Microscopy pictures were taken using an EVOS FL cell imaging system (Thermo Fisher Scientific).

Transwell assay

Tumors from mice were passed through a 70 μm cell strainer (Falcon) to obtain a single-cell suspension. CD11b$^+$ cells were isolated using CD11b magnetic beads (BioLegend, 480109) and further enriched for F4/80$^+$ macrophages using F4/80 beads (BioLegend, 480169), NK cells using the mouse NK cell isolation kit (BioLegend, 480049, 5 μl/1 million cells of biotin, 10 μl/1 million cells of nanobeads) or DCs using Mouse Pan Dendritic Cell Isolation Kit (BioLegend, 480097, 10 μl/1 million cells of biotin, 10 μl/1 million cells of nanobeads).

For murine macrophage–NK migration assays, F4/80$^+$ macrophages were plated in the bottom chamber and stimulated with 40 MOI of adenovirus. NK cells were fluorescently labeled with 5 μM CellTracker™ Green CMFDA Dye (Thermo Fisher Scientific, Cat#C2925) and seeded in the upper chamber of 6.5 mm Transwell® polycarbonate membrane inserts with 5.0 μm pore size (Corning). Where indicated, NK cells were pre-incubated with 10 μg/ml of anti-mouse CXCR3 antibody (BioXcell, Cat#BE0249) prior to migration. After 24 h, migrated NK cells were quantified using a BD LSRFortessa (BD Biosciences) with Precision Count Beads™ (BioLegend, Cat#424902, 5 μl per sample).

For murine NK–DC migration assays, NK cells were isolated from the TME using the NK cell isolation kit (BioLegend, 480049, 5 μl/1 million cells of biotin, 10 μl/1 million cells of nanobeads), while DCs were isolated using the MojoSort™ Mouse Pan Dendritic Cell Isolation Kit (BioLegend, 480097, 10 μl/1 million cells of biotin, 10 μl/1 million cells of nanobeads). Where indicated, NK cells were stimulated with 1 μg/ml of WPG overnight and then washed with PBS. DCs were labeled with 5 μM CellTracker™ Green CMFDA Dye and placed in the upper chamber of Transwell® inserts (5.0 μm). NK cells were plated in the

lower chamber and stimulated with 40 MOI of adenovirus. In selected conditions, NK cells were treated with 10 μg/ml of anti-CCL5 antibody (BioXcell, Cat#BE0449) prior to migration. After 24 hours, migrated DCs were quantified by flow cytometry on a BD LSRFortessa using Precision Count Beads™.

ChIP-qPCR on murine samples

Chromatin immunoprecipitation (ChIP) was performed to assess H3K4me3 enrichment at target loci. Briefly, 1×10^7 cells were cross-linked in culture with 0.75% formaldehyde for 10 min at room temperature, followed by quenching with 125 mM glycine for 5 min. Cells were washed twice in cold PBS, collected by scraping, pelleted, and resuspended in FA lysis buffer (750 μl per 1×10^7 cells). Nuclei were disrupted by sonication for 15 cycles (1 min ON and 1 min OFF) for murine samples while for human samples 25 cycles (1 min ON and 1 min OFF) to generate chromatin fragments of 500–1,000 bp, confirmed on a 1.5% agarose gel. Input samples were saved prior to immunoprecipitation.

For ChIP, 25 μg protein per reaction was diluted 1:10 in RIPA buffer and incubated overnight at 4 °C with anti-H3K4me3 antibody or with control IgG antibody (1 μg antibody per 25 μg protein) and Protein A/G beads (pre-blocked with herring sperm DNA and BSA). Bead-only samples served as negative controls. Beads were sequentially washed three times with wash buffer and once with final wash buffer before elution in 120 μl elution buffer. Cross-links were reversed at 65 °C for 4–5 h with RNase A and proteinase K treatment. DNA was purified using a PCR purification kit (Qiagen) according to the manufacturer's instructions.

Purified DNA was analyzed by quantitative PCR using primers specific for target promoters (e.g., CXCL9, CXCL10, *Slc6a8*). Ct values from immunoprecipitated samples were first corrected by subtracting IgG background. Data were then normalized to input DNA to account for differences in chromatin quantity. Enrichment was expressed as fold enrichment relative to control samples (non-trained). Primer can be found in Supplementary Table 1.

RT-qPCR

NK cells were isolated from mouse tumors using the MojoSort™ Mouse NK Cell Isolation Kit (BioLegend, Cat#480049) according to the manufacturer's instructions. Total RNA was extracted using the RNeasy Mini Kit (Qiagen, Cat#74104), and RNA concentration and purity were determined using a NanoDrop spectrophotometer (Thermo Fisher Scientific). For cDNA synthesis, RNA sample was reverse transcribed using Maxima Reverse Transcriptase (200 U/μL; Thermo Fisher Scientific, Cat#EP0742) following the manufacturer's protocol.

Quantitative PCR (qPCR) was performed using GoTaq® qPCR Master Mix (Promega, Cat#A6002) on a QuantStudio 5 Real-Time PCR System (Applied Biosystems). Each reaction was run in technical triplicates with the following cycling conditions: 95 °C for 2 min, followed by 40 cycles of 95 °C for 15 s and 60 °C for 1 min. Expression levels were normalized to *Gapdh*, and fold change was calculated using the ΔΔCt method relative to PBS-treated NK cell controls. Primer can be found in Supplementary Table 1.

Long-term generation of peptide-specific CD8 + T cells

Isolated PBMCs were trained using PBS or 1 μg/mL of WPG for 24 h. Trained PBMCs were cultured with GM-CSF (1000 U/mL) and IL-4 (800 U/mL) for 4 days to differentiate into monocyte-derived dendritic cells (moDCs). To stimulate peptide-specific T cells, PBMCs were pulsed with PC (10 μM of peptides complexed with 10^9 viral particles). Subsequently, TNFα (10 ng/mL, Peprotech) and LPS (10 ng/mL) were directly applied which were incubated for 4 h to generate semi-mature dendritic cells. After, IL-21 (60 ng/mL, Peprotech) was added to enhance T-cell expansion. After 10–12 days, the T cells were re-stimulated with PC for an additional 10 days. The cultures were maintained by feeding every 2–3 days with IL-2 (50 U/mL, STEMCELL Technologies).

Short-term generation of peptide-specific CD8 + T cells

10^6 PBMCs were plated in a 24-well plate and treated with PBS or 1 μg/mL of WPG for 24 h. Cells were then washed and stimulated with PC (10 μM of peptides complexed with 10^9 viral particles). After three days, IL-2 (50 U/mL, STEMCELL Technologies) was added to further expand T cells. PBMCs were then restimulated with PC and treated with brefeldin A (1:1,000) and monensin A (1:1,000) at 37 °C for 5 h.

Microscopy and quantification

Microscopy visualization of PDO killing was conducted with EVOS M7000 Imaging System (Thermo Fisher Scientific) where images of green labeled CD8 + T-cells and cell death (using PI) were obtained in the transmitted, Green Fluorescent Protein (GFP) and Red Fluorescent Protein (RFP) channels respectively. Settings including brightness, focus and counts per image were established manually, with the desired targets per image. After manual calibration automated image acquisition was performed to obtain 50 images per well across multiple channels and build a Z-stack. Automated image acquisition for this study included transmitted (for conventional colored precipitate product), RFP and GFP.

Metabolomic profiling

Sorted CD11b+ cells from murine tumors were add to 400 μl of cold extraction solvent, followed immediately by centrifugation at 14,000 rpm for 5 minutes at 4 °C. The supernatants were then loaded onto an Ostro 96-well plate (25 mg; Waters) and processed using a robotic vacuum. The resulting filtrates were transferred into polypropylene tubes and dried completely in a nitrogen gas evaporator. The dried residues were reconstituted in 40 μl of extraction solvent, vortexed for 2 minutes, and then transferred into HPLC glass autosampler vials. Two microliters of each sample were injected into a Thermo Vanquish UHPLC system coupled with a Q-Exactive Orbitrap quadrupole mass spectrometer fitted with a heated electrospray ionization (H-ESI) source (Thermo Fisher Scientific). Chromatographic separation was performed using a SeQuant ZIC-pHILIC column (2.1 mm × 100 mm, 5 μm particle size; Merck) under gradient elution at a flow rate of 0.100 ml/min. Mobile phase A, composed of 20 mM ammonium hydrogen carbonate adjusted to pH 9.4 with a 25% ammonium solution, and acetonitrile as mobile phase B were used in the following gradient: starting at 20% A and 80% B, maintained until 2 minutes, then gradually increasing mobile phase A to 80% by 17 minutes, and finally reducing back to 20% A at 17.1 minutes, which was held until 24 minutes. The column oven and autosampler were maintained at 40° ± 3 °C and 5° ± 3 °C, respectively. Mass spectrometry was performed with polarity switching under the following conditions: a resolution of 35,000; spray voltages of 4250 V (positive mode) and 3250 V (negative mode); sheath gas at 25 arbitrary units; auxiliary gas at 15 arbitrary units; sweep gas flow of 0; capillary temperature at 275 °C; and an S-lens RF level of 50.0. The instrument was operated using Xcalibur 4.1.31.9 software (Thermo Fisher Scientific), and metabolites were annotated for 462 metabolites with TraceFinder 4.1 software (Thermo Fisher Scientific) using mass to charge ratios and retention time of standards (MSMLS-1EA, Merck). Throughout the run, the data quality was monitored by including a pooled serum quality control (QC) sample every 10th injection. The final data was prefiltered for metabolites having poor chromatograph, high variation in pooled QC samples > 20% RSD or background noise > 20% when compared to blank samples. Data was analysed with MetaboAnalyst 5.0 (https://www.metaboanalyst.ca/). Missing variables were imputed by replacing with 1/5 of the minimum positive values of individual features. The data was further normalized with log10-transformation and

auto-scaling. In multivariate clustering analysis the heatmap was computed using distance measure euclidean for up to 25 most significant features (t-test). Principal component analysis (PCA) was used to visualize the data. For Univariate analysis t-test and volcano plot analysis were performed with fold change1.5 and raw p-value < 0.05. Quantitative metabolite set enrichment analysis (MSEA) was performed in the MetaboAnalyst 5.0 using the mouse KEGG database.

Hashting samples for Single-cell RNA sequencing

Sorted CD11b$^+$ cells were washed 2–3 times with 10 mL of PBS and then resuspended in 100 µL of Cell Staining Buffer (BioLegend, Cat# 420201). Next, 10 µL of TruStain FcX blocking reagent (BioLegend, Cat# 420510) was added, and the cells were incubated for 10 minutes to block non-specific binding. A unique TotalSeq-A hashing antibody (BioLegend, Cat#1603-1608, 1 µl/1 million cells) was then added to each sample at a concentration of 1–2 µL (or 1–2 µg per sample) and incubated for 30 min at 4 °C in the dark. Following this, the cells were washed 3–5 times with 3 mL of staining buffer, combined into a single 1 mL volume of staining buffer, centrifuged, and finally resuspended in PBS containing 0.04% bovine serum albumin (BSA) before proceeding to scRNA-seq.

Single-cell RNA sequencing

The Chromium Single Cell 3′RNAseq run and library preparations were performed using the 10x Genomics Chromium Next GEM Single Cell 3′ Gene Expression v3.1 Dual Index chemistry, with modifications outlined by Stoeckius et al.22 (https://cite-seq.com/) and based on an updated protocol available at www.biolegend.com/en-us/protocols/totalseq-a-antibodies-and-cell-hashing-with-10x-single-cell-3-reagent-kit-v3-3-1-protocol. Approximately 15,000 cells were aimed per 10x lane (GEM well) that contained hashed samples from 13 cell lines, which were cultured either alone or in combination with NK cells, with separate GEM wells allocated for each treatment group. This setup resulted in targeting roughly 1000–1200 cells for sequencing from each cell line in mono- or co-culture. The 3′ GEX and Cell Hashing (multiplexing) libraries were sequenced on an Illumina NovaSeq 6000 system, with read lengths set at 28 bp for Read 1, 10 bp for the i7 Index, 10 bp for the i5 Index, and 90 bp for Read 2.

Single-Cell RNA sequencing analysis

scRNA-seq data were processed using Seurat (v6.0) in R (v4.3.2). For quality control, cells were filtered to exclude those with < 200 or > 2500 detected genes, > 30% mitochondrial gene content, or genes expressed in fewer than three cells. Cells with abnormally high ribosomal content (> 50%) or low UMI counts (< 700) were also removed.

Gene expression values were normalized with the NormalizeData function using the LogNormalize method (scaling factor = 10,000). Highly variable genes (HVGs; $n = 2000$) were identified using the "vst" method in FindVariableFeatures. Data were scaled and centered using the ScaleData function. To control for cell-cycle heterogeneity, cell-cycle scores were computed with CellCycleScoring (G2/M and S markers provided in Seurat) and regressed out during scaling.

Dimensionality reduction was performed by principal component analysis (PCA) on HVGs. The top 30 PCs were selected based on elbow plot inspection and JackStraw resampling. To mitigate batch effects across experiments, we applied Harmony (v1.0) with default parameters, using sample identity as the covariate.

Clustering was performed using the FindNeighbors and FindClusters functions. For global clustering across all immune cells, we used a resolution of 0.5; for lymphoid cell-focused subclustering, a resolution of 0.5 was applied; and for TAM/monocyte analyses, we used 0.4. Two-dimensional visualization was performed with UMAP (RunUMAP, 30 PCs, default settings).

Cluster annotation was guided by differentially expressed (DE) markers, identified with the FindAllMarkers function (Wilcoxon rank-sum test, log2 fold-change > 0.8 or <−0.8, adjusted p value < 0.05, Bonferroni correction). Differential expression between experimental groups was performed with the FindMarkers function using the same thresholds. Cell type identities were then assigned by manual review of cluster-specific DEGs and confirmed using the ImmGen MyGeneSet tool, rather than automated classification tools, to ensure biologically grounded annotations.

Tissue collection for PDO culture and ethical perimits

Tissue samples were obtained by surgeon either via endoscopic biopsy forceps or via biopsy from surgical specimen. The samples were transported to the laboratory in a transfer medium (DMEM supplemented with 1% Penicillin-Streptomycin solution) and processed within 24 h after collection. The iCAN Flagship Project biobank study is based on a biobank consent and was reviewed by the HUS Ethical Committee and is executed based on a HUS research permit (4.5.2023 §38 (HUS/223/2023), a Findata data permit (THL/1338/14.02.00/2022), and MTAs with Helsinki Biobank (HBP20210170) and Finnish Hematology and Registry Biobank FHRB (12.5.2022). All samples used in this study were destroyed after the analysis.

PDO culture

Tissue samples were dissociated mechanically by P1000 pipette, followed, if necessary, by a ten-minute enzymatic digestion with Organoid Digestion Medium to increase biomass output. Dissociated cells were washed 1 or 3 (in case of enzymatic digestion) times by centrifugation (5 min at 4 °C, 200 g) in Wash medium, resuspended in Matrigel (Corning, Cat# 354230) and plated as a single domes (50 µL each) on a 24-well plate (1 dome/well). After Matrigel solidifying (15-30 min in 37 °C), 500 µL of Organoid Culture Medium supplemented with 1 µL/mL Rho-associated coiled-coil kinase inhibitor Y-27632 was added to cover the domes, and plates were returned to 37 °C (with 21% O2 and 5% CO2) and cultured for expansion. Organoid Culture Medium was changed every 7 days. Organoids were passaged every 14 days (or 7 days if necessary).

T-cell killing assays with PDOs

CRC PDOs were co-cultured with 100,000 expanded CD8 + T-cells. CD8 + T cells were injected using a 27 G needle straight into the matrigel. Propidium iodide was added (1:1000) to the culture to visualize death. After 24 h of incubation at 37 °C, cell killing was measured by determining the amount of LDH released using a colometric assay (CyQUANT LDH Cytotoxicity Assay, Cat# C20303). Specific lysis was then calculated using the following formula: Percent cytotoxicity = ("experimental"−"target spontaneous")/("target maximum"−"target spontaneous") × 100%, where "experimental" corresponds to the signal measured in a treated sample, "target spontaneous" corresponds to the signal measured in PDOs alone and "target maximum" corresponds to the signal measured in the presence of detergent lysed tumor cells.

Reporting summary

Further information on research design is available in the Nature Portfolio Reporting Summary linked to this article.

Data availability

All scRNA sequencing data generated in this study have been deposited in the Genome Sequence Archive (GSA) under the accession number **CRA024974** (https://ngdc.cncb.ac.cn/gsa/browse/CRA024974). The full dataset of the metabolomics data can be found in the Source Data (Supplementary Fig. 7A). The remaining data supporting the findings of this study are available within the Article or

its Supplementary Information. Source data are provided with this paper.

References

1. Siegel, R. L., Miller, K. D., Fuchs, H. E. & Jemal, A. Cancer statistics, 2021. *CA Cancer J. Clin.* **71**, 7–33 (2021).
2. Morgan, E. et al. Global burden of colorectal cancer in 2020 and 2040: incidence and mortality estimates from GLOBOCAN. *Gut* **72**, 338–344 (2023).
3. Sung, H. et al. Colorectal cancer incidence trends in younger versus older adults: an analysis of population-based cancer registry data. *Lancet Oncol.* **26**, 51–63 (2025).
4. Mariotto, A. B., Thompson, T. D., Johnson, C., Wu, X. C. & Pollack, L. A. Breast and colorectal cancer recurrence-free survival estimates in the US: modeling versus active data collection. *Cancer Epidemiol.* **85**, 102370 (2023).
5. Yan, S. et al. Immune checkpoint inhibitors in colorectal cancer: limitation and challenges. *Front Immunol.* **15**, 1403533 (2024).
6. Moreau, M. et al. A multicenter study evaluating efficacy of immune checkpoint inhibitors in advanced non-colorectal digestive cancers with microsatellite instability. *Eur. J. Cancer* **202**, 959–8049 (2024).
7. André, T., Cohen, R. & Salem, M. E. Immune checkpoint blockade therapy in patients with colorectal cancer harboring microsatellite instability/mismatch repair deficiency in 2022. *American Society of Clinical Oncology Educational Book* 233–241 https://doi.org/10.1200/EDBK_349557 (2022).
8. Yamaguchi, K. et al. Efficacy of pembrolizumab in microsatellite-stable, tumor mutational burden-high metastatic colorectal cancer: genomic signatures and clinical outcomes. *ESMO Open* **10**, 104108 (2025).
9. Galon, J. et al. Type, density, and location of immune cells within human colorectal tumors predict clinical outcome. *Science* **313**, 1960–1964 (2006).
10. Le, D. T. et al. Mismatch-repair deficiency predicts response of solid tumors to PD-1 blockade. *Science* **357**, 409 (2017).
11. Hazama, S. et al. A phase II study of five peptides combination with oxaliplatin-based chemotherapy as a first-line therapy for advanced colorectal cancer (FXV study). *J. Transl. Med.* **12**, 108 (2014).
12. Murahashi, M. et al. Phase I clinical trial of a five-peptide cancer vaccine combined with cyclophosphamide in advanced solid tumors. *Clin. Immunol.* **166–167**, 48–58 (2016).
13. Harris, J. E. et al. Adjuvant active specific immunotherapy for stage II and III colon cancer with an autologous tumor cell vaccine: Eastern Cooperative Oncology Group study E5283. *J. Clin. Oncol.* **18**, 148–157 (2000).
14. Toh, H. C. et al. Clinical benefit of allogeneic melanoma cell lysate-pulsed autologous dendritic cell vaccine in mage-positive colorectal cancer patients. *Clin. Cancer Res.* **15**, 7726–7736 (2009).
15. Saito, T. et al. Two FOXP3+CD4+ T cell subpopulations distinctly control the prognosis of colorectal cancers. *Nat. Med.* **22**, 679–684 (2016).
16. Loddenkemper, C. et al. In situ analysis of FOXP3+ regulatory T cells in human colorectal cancer. *J. Transl. Med.* **4**, 1–8 (2006).
17. Bonertz, A. et al. Antigen-specific Tregs control T cell responses against a limited repertoire of tumor antigens in patients with colorectal carcinoma. *J. Clin. Invest.* **119**, 3311 (2009).
18. Zhang, B. et al. Circulating and tumor-infiltrating myeloid-derived suppressor cells in patients with colorectal carcinoma. *PLoS One* **8**, e57114 (2013).
19. Brandau, S., Moses, K. & Lang, S. The kinship of neutrophils and granulocytic myeloid-derived suppressor cells in cancer: cousins, siblings or twins?. *Semin Cancer Biol.* **23**, 171–182 (2013).
20. Wang, P. F. et al. Prognostic role of pretreatment circulating MDSCs in patients with solid malignancies: a meta-analysis of 40 studies. *Oncoimmunology* **7**, e1494113 (2018).
21. Li, J. et al. Tumor-associated macrophage infiltration and prognosis in colorectal cancer: systematic review and meta-analysis. *Int J. Colorectal Dis.* **35**, 1203–1210 (2020).
22. Zhou, Q. et al. The density of macrophages in the invasive front is inversely correlated to liver metastasis in colon cancer. *J. Transl. Med.* **8**, 13 (2010).
23. Forssell, J. et al. High macrophage infiltration along the tumor front correlates with improved survival in colon cancer. *Clin. Cancer Res.* **13**, 1472–1479 (2007).
24. Koelzer, V. H. et al. Phenotyping of tumor-associated macrophages in colorectal cancer: Impact on single cell invasion (tumor budding) and clinicopathological outcome. *Oncoimmunology* **5**, e1106677 (2015).
25. Zhu, Q., Han, X., Peng, J., Qin, H. & Wang, Y. The role of CXC chemokines and their receptors in the progression and treatment of tumors. *J. Mol. Histol.* **43**, 699–713 (2012).
26. Johnson, D. E., O'Keefe, R. A. & Grandis, J. R. Targeting the IL-6/JAK/STAT3 signalling axis in cancer. *Nat. Rev. Clin. Oncol.* **15**, 234 (2018).
27. Zhang, Y., Rajput, A., Jin, N. & Wang, J. Mechanisms of immunosuppression in colorectal cancer. *Cancers (Basel)* **12**, 3850 (2020).
28. Netea, M. G. et al. Defining trained immunity and its role in health and disease. *Nat. Rev. Immunol.* **20**, 375–388 (2020). *2020 20:6*.
29. Ciarlo, E. et al. Trained immunity confers broad-spectrum protection against bacterial infections. *J. Infect. Dis.* **222**, 1869 (2019).
30. Moorlag, S. J. C. F. M. et al. β-Glucan induces protective trained immunity against Mycobacterium tuberculosis infection: a key role for IL-1. *Cell Rep.* **31**, 107634 (2020).
31. Ciarlo, E. et al. Trained immunity confers broad-spectrum protection against bacterial infections. *J. Infect. Dis.* **222**, 1869–1881 (2020).
32. Khan, N. et al. β-Glucan reprograms neutrophils to promote disease tolerance against influenza A virus. *Nat. Immunol.* **26**, 174–187 (2025).
33. Starr, S. E., Visintine, A. M., Tomeh, M. O. & Nahmias, A. J. Effects of immunostimulants on resistance of newborn mice to herpes simplex type 2 infection. *Proc. Soc. Exp. Biol. Med.* **152**, 57–60 (1976).
34. Suenaga, T., Okuyama, T., Yoshida, I. & Azuma, M. Effect of Mycobacterium tuberculosis BCG infection on the resistance of mice to ectromelia virus infection: participation of interferon in enhanced resistance. *Infect. Immun.* **20**, 312–314 (1978).
35. Spencer, J. C., Ganguly, R. & Waldman, R. H. Nonspecific protection of mice against influenza virus infection by local or systemic immunization with bacille calmette-guerin. *J. Infect. Dis.* **136**, 171–175 (1977).
36. Floc'h, F. & Werner, G. H. Increased resistance to virus infections of mice inoculated with BCG (Bacillus calmette-guérin). *Ann. Immunol. (Paris)* **127**, 173–186 (1976).
37. Masuda, Y., Yamashita, S., Nakayama, Y., Shimizu, R. & Konishi, M. Maitake beta-glucan enhances the therapeutic effect of trastuzumab via antibody-dependent cellular cytotoxicity and complement-dependent cytotoxicity. *Biol. Pharm. Bull.* **47**, 840–847 (2024).
38. Kalafati, L. et al. Innate immune training of granulopoiesis promotes anti-tumor activity. *Cell* **183**, 771–785.e12 (2020).
39. Wattenberg, M. M. et al. Cancer immunotherapy via synergistic coactivation of myeloid receptors CD40 and Dectin-1. *Sci. Immunol.* **8**, eadj5097 (2023).
40. Geller, A. E. et al. The induction of peripheral trained immunity in the pancreas incites anti-tumor activity to control pancreatic cancer progression. *Nat. Commun.* **13**, 1–20 (2022).
41. Feola, S. et al. Peptides-Coated Oncolytic Vaccines for Cancer Personalized Medicine. *Front Immunol.* **13**, 826164 (2022).

42. Capasso, C. et al. Oncolytic adenoviruses coated with MHC-I tumor epitopes increase the antitumor immunity and efficacy against melanoma. *Oncoimmunology* **5**, e1105429 (2015).
43. Lee, H. G., Cho, M. Z. & Choi, J. M. Bystander CD4+ T cells: crossroads between innate and adaptive immunity. *Exp. Mol. Med.* **52**, 1255–1263 (2020).
44. Feola, S. et al. A novel immunopeptidomic-based pipeline for the generation of personalized oncolytic cancer vaccines. *Elife* **11**, e71156 (2022).
45. Dufva, O. et al. Single-cell functional genomics reveals determinants of sensitivity and resistance to natural killer cells in blood cancers. *Immunity* **56**, 2816–2835.e13 (2023).
46. Barry, K. C. et al. A natural killer-dendritic cell axis defines checkpoint therapy-responsive tumor microenvironments. *Nat. Med* **24**, 1178–1191 (2018).
47. Böttcher, J. P. et al. NK cells stimulate recruitment of cDC1 into the tumor microenvironment promoting cancer immune control. *Cell* **172**, 1022–1037.e14 (2018).
48. Ray, A. et al. Targeting CD206+ macrophages disrupts the establishment of a key antitumor immune axis. *J. Exp. Med.* **222**, e20240957 (2025).
49. Broz, M. L. et al. Dissecting the tumor myeloid compartment reveals rare activating antigen-presenting cells critical for T cell immunity. *Cancer Cell* **26**, 938 (2014).
50. Doedens, A. L. et al. Macrophage expression of hypoxia-inducible factor-1α suppresses T-cell function and promotes tumor progression. *Cancer Res.* **70**, 7465–7475 (2010).
51. Mitchem, J. B. et al. Targeting tumor-infiltrating macrophages decreases tumor-initiating cells, relieves immunosuppression, and improves chemotherapeutic responses. *Cancer Res.* **73**, 1128–1141 (2013).
52. Nixon, B. G. et al. Tumor-associated macrophages expressing the transcription factor IRF8 promote T cell exhaustion in cancer. *Immunity* **55**, 2044–2058.e5 (2022).
53. Park, M. D. et al. TREM2 macrophages drive NK cell paucity and dysfunction in lung cancer. *Nat. Immunol.* **24**, 792–801 (2023).
54. Peranzoni, E. et al. Macrophages impede CD8 T cells from reaching tumor cells and limit the efficacy of anti–PD-1 treatment. *Proc. Natl. Acad. Sci. USA* **115**, E4041–E4050 (2018).
55. Ruffell, B. et al. Macrophage IL-10 blocks CD8+ T cell-dependent responses to chemotherapy by suppressing IL-12 expression in intratumoral dendritic cells. *Cancer Cell* **26**, 623–637 (2014).
56. Subtil, B., Cambi, A., Tauriello, D. V. F. & de Vries, I. J. M. The therapeutic potential of tackling tumor-induced dendritic cell dysfunction in colorectal cancer. *Front Immunol.* **12**, 724883 (2021).
57. Zhu, B. et al. Plasticity of Ly-6Chi myeloid cells in T cell regulation. *J. Immunol.* **187**, 2418 (2011).
58. Ramachandran, P. et al. Differential Ly-6C expression identifies the recruited macrophage phenotype, which orchestrates the regression of murine liver fibrosis. *Proc. Natl. Acad. Sci. USA* **109**, E3186–E3195 (2012).
59. Mantovani, A., Marchesi, F., Malesci, A., Laghi, L. & Allavena, P. Tumour-associated macrophages as treatment targets in oncology. *Nat. Rev. Clin. Oncol.* **14**, 399–416 (2017).
60. Ferreira, A. V., Domínguez-Andrés, J., Merlo Pich, L. M., Joosten, L. A. B. & Netea, M. G. Metabolic regulation in the induction of trained immunity. *Semin Immunopathol.* **46**, 7 (2024).
61. Peng, Z. & Saito, S. Creatine supplementation enhances anti-tumor immunity by promoting adenosine triphosphate production in macrophages. *Front Immunol.* **14**, 1176956 (2023).
62. Bhagat, A., Lyerly, H. K., Morse, M. A. & Hartman, Z. C. CEA vaccines. *Hum. Vaccin Immunother.* **19**, 2291857 (2023).
63. Evers, M. et al. Novel chimerized IgA CD20 antibodies: Improving neutrophil activation against CD20-positive malignancies. *MAbs* **12**, 1795505 (2020).

Acknowledgements

The flow cytometry analysis was performed at the HiLife Flow Cytometry Unit, University of Helsinki. We acknowledge the Helsinki Metabolomics Center, supported by HiIFE and Biocenter Finland. The single-cell RNA sequencing was performed with FIMM Single-Cell Analytics and Sequencing units supported by HiLIFE and Biocenter Finland. We are also grateful for Dr. Cristian Smerdou (Cima Universidad de Navarra) for kindly gifting us the MC38 cell line. We would also like to acknowledge bachelor student, Karim Hamdan, for helping in some experiments. This work has been supported by European Research Council (ERC), Horizon 2020 (H2020) framework (Agreement No. 681219) (V.C.), Magnus Ehrnrooth Foundation (project No. 4706235) (V.C.), Jane and Aatos Erkko Foundation (Project No. 4705796) (V.C.), Finnish Cancer Foundation (project No. 4706116) (V.C.), Helsinki Institute of Life Science (HiLIFE) (project No. 797011004) (V.C.), Digital Precision Cancer Medicine Flagship iCAN (V.C.), GeneCellNano flagship (V.C.), HiLIFE HiPOC (FH), Research Council of Finland (TTS) and iCAN Digital Precision Cancer Medicine Flagship (TTS), and research grants by Jane and Aatos Erkko Foundation (TTS), Sigrid Juselius Foundation (TTS), Mary and Georg Ehrnrooth Foundation (TTS), Cancer Foundation Finland (TTS), Relander Foundation (TTS), and HUS(TTS) and Pirha state research funding (TTS).

Author contributions

S.G. and F.D have contributed equally to this work. Specific contributions: Conceptualization: F.H, S.G and V.C. Investigation: F.H, S.G, F.D, Y.G, J.K, M.Fu, E.Z, S.R, O.I, P.B, J.C, G.A, M.Fe, V.S, M.S, J.S, A.N, O.E, KM.A. Data Curation: F.H., S.G., A.I.N., and F.D. Formal analysis. F.H., S.G., A.I.N., F.D and V.C. Visualization: F.H. Project administration: F.H. and V.C. Writing original draft: F.H., S.G., M.G. and V.C. Writing-Review editing: All authors. Funding acquisition: N.Z, O.E, S.M, T.TS, M.G and V.C

Competing interests

V.C. is co-founder and shareholder of Valo Therapeutics LTD. H.C. and L.K. are stakeholders of Valo Therapeutics LTD. Toni T. Seppälä reports consultation fees from Mehiläinen, Nouscom, Orion Pharma, Amgen, and Tillots Pharma, and a position in the Clinical Advisory Board and as a minor shareholder of Lynsight Ltd. S.M. has received honoraria and research funding from Novartis, Pfizer, and Bristol-Myers Squibb and honoraria from Dren-Bio (not related to this study). V.S. is an employee and shareholder of AstraZeneca. All other named authors declare that they have no competing interests, financial or otherwise.

Additional information

Supplementary information The online version contains supplementary material available at https://doi.org/10.1038/s41467-026-68466-5.

Correspondence and requests for materials should be addressed to Vincenzo Cerullo.

Peer review information *Nature Communications* thanks Xiaojun Xia, Jun Yan, and the other, anonymous, reviewer(s) for their contribution to the peer review of this work. A peer review file is available.

[1]Drug Research Program (DRP) ImmunoViroTherapy Lab (IVT), Division of Pharmaceutical Biosciences, Faculty of Pharmacy, Viikinkaari 5E, University of Helsinki, Helsinki, Finland. [2]Helsinki Institute of Life Science (HiLIFE), Fabianinkatu 33, University of Helsinki, Helsinki, Finland. [3]Translational Immunology Program (TRIMM), Faculty of Medicine Helsinki University, Haartmaninkatu 8, University of Helsinki, Helsinki, Finland. [4]iCAN Digital Precision Cancer Medicine Flagship, Helsinki, Finland. [5]Translational Immunology Research Program and Department of Clinical Chemistry and Hematology, University of Helsinki, Helsinki, Finland. [6]Hematology Research Unit Helsinki, Helsinki University Hospital Comprehensive Cancer Center, Helsinki, Finland. [7]Applied Tumor Genomics Research, Research Program Unit, University of Helsinki, Helsinki, Finland. [8]Department of Molecular Medicine and Medical Biotechnology, Naples University "Federico II", S. Pansini 5, Naples, Italy. [9]Department of Molecular Medicine and Medical Biotechnology and CEINGE, Naples University Federico II, Naples, Italy. [10]Biochemistry/Developmental Biology, Faculty of Medicine, University of Helsinki, Helsinki, Finland. [11]Institute for Molecular Medicine Finland (FIMM), Helsinki Institute of Life Science (HiLIFE), University of Helsinki, Helsinki, Finland. [12]Cell Therapy Safety, Clinical and Pharmacological Safety Sciences, AstraZeneca R&D, Pepparedsleden 1, Mölndal, Sweden. [13]Helsinki Metabolomics Center, Stem Cell and Metabolism Research Program, Faculty of Medicine, University of Helsinki, Helsinki, Finland. [14]Faculty of Medicine and Health Technology, Tampere University and Tays Cancer Centre, Tampere University Hospital, Tampere, Finland. [15]Department of Gastrointestinal Surgery, Helsinki University Central Hospital, University of Helsinki, Helsinki, Finland. [16]These authors contributed equally: Sara Gandolfi, Federica D'Alessio. ✉e-mail: vincenzo.cerullo@helsinki.fi